A NUMERICAL ALGORITHM TO MODEL WALL SLIP AND CAVITATION IN TWO-DIMENSIONAL HYDRODYNAMICALLY LUBRICATED CONTACTS

A THESIS SUBMITTED TO

THE GRADUATE SCHOOL OF ENGINEERING AND SCIENCE

OF BILKENT UNIVERSITY

IN PARTIAL FULFILLMENT OF THE REQUIREMENTS FOR

THE DEGREE OF

MASTER OF SCIENCE

IN

MECHANICAL ENGINEERING

By

Mert Yusuf Çam

January 2022

A NUMERICAL ALGORITHM TO MODEL WALL SLIP AND CAVITATION IN TWO-DIMENSIONAL HYDRODYNAMICALLY LUBRICATED CONTACTS

By Mert Yusuf Çam

January 2022

We certify that we have read this thesis and that in our opinion it is fully adequate, in scope and in quality, as a thesis for the degree of Master of Science.

Luca Biancofiore(Advisor)

Matteo Giacopini

İlker Temizer

Approved for the Graduate School of Engineering and Science:

Ezhan Karaşan
Director of the Graduate School

ABSTRACT

A NUMERICAL ALGORITHM TO MODEL WALL SLIP AND CAVITATION IN TWO-DIMENSIONAL HYDRODYNAMICALLY LUBRICATED CONTACTS

Mert Yusuf Çam
M.S. in MECHANICAL Engineering
Advisor: Luca Biancofiore
January 2022

Hydrodynamic lubrication takes a fundamental role in mechanical systems to reduce energy losses and prevent mechanical breakdown. In order to model hydrodynamic lubrication in thin films the solution of the Reynolds equation is required. However, the Reynolds equation cannot reflect all the lubricant characteristics in thin films. The effects of two critical factors, wall slip and cavitation, need to be considered. A new numerical solution of the Reynolds equation is presented to model two-dimensional hydrodynamic lubrication, including the linear complementary mass-conserving cavitation model and multi-linearity wall slip model. In addition, a new wall slip model has been proposed by modifying the multi-linearity wall slip model to make it more computationally affordable. The proposed mathematical model has been validated against available models in literature with the tests performed on journal bearings, slider bearings, squeeze dampers, and surface textured bearings. The proposed novel wall slip model is up to 9 times more computational affordable than the original multi-linearity wall slip model.

Keywords: hydrodynamic lubrication, cavitation, boundary slippage, wall slip.

ÖZET

HİDRODİNAMİK OLARAK YAĞLANMIŞ TEMASLARDA DUVAR KAYMASI VE KAVİTASYONU MODELLEMEK İÇİN İKİ BOYUTLU SAYISAL ALGORİTMA

Mert Yusuf Çam
Makine Mühendisliği, Yüksek Lisans
Tez Danışmanı: Luca Biancofiore
Ocak 2022

Hidrodinamik yağlama, enerji kayıplarını azaltmak ve yüzeylerdeki aşınmayı önlemek için mekanik sistemlerde temel bir rol oynar. İnce filmlerde hidrodinamik yağlamayı modellemek için Reynolds denkleminin çözümü gereklidir. Ancak Reynolds denklemi, ince filmlerdeki yağlayıcının tüm özelliklerini yansıtamaz. Yüzey kayması ve kavitasyon gibi iki kritik faktörün etkilerinin dikkate alınması gerekmektedir. İki boyutlu hidrodinamik yağlamayı modellemek için kütlenin korunduğu doğrusal tamamlayıcı kavitasyon modeli ve çok doğrusallıklı yüzey kayma modelinin Reynolds denklemine dahil edildiği yeni bir sayısal çözüm sunulmaktadır. Ek olarak, çoklu doğrusallıklı yüzey kayma modelinde bir değişiklik yapılarak, sayısal hesaplama açısından daha uygun maliyetli yeni bir yüzey kayma modeli önerilmiştir. Önerilen matematiksel modeller, rulman yatakları, sıkıştırılan damperler ve yüzeyi dokulu yataklar üzerinde yapılan testlerin sonuçlarının literatürdeki mevcut modellerle kısyaslanması ile doğrulanmıştır. Önerilen yeni yüzey kayma modeli, orijinal çoklu doğrusallıklı yüzey kayma modelinden 9 kata kadar daha hızlıdır.

Anahtar sözcükler: hidrodinamik yağlama, kavitasyon, yüzey kayması.

Acknowledgement

First of all, I would like to express my deepest gratitude and thanks to Dr. Luca Biancofiore for giving me the opportunity to be part of the FluidFrame research group and to be able to work with him on this project. Throughout my studies, he not only helped and guided me, but also gave me motivation and vision to become a better researcher and engineer.

I would like to express my sincere gratitude to Dr. Matteo Giacopini for his assistance, recommendations and valuable discussions during this project.

I would like to thank Berfin Karabulut for always supporting and being there for me when I needed motivation and energy the most.

Special thanks to my friends Dursun Karaca Erdemir, Abdullah Mert Şahin, Ekin Deniz Yıldız, Mete Nikita Myagkiy, Aylin Bahar Ergül, Uğur Can Özdemir, Utku Hatipoğlu, Cem Aydoğan, İlhami Ilgaz Aydoğdu, Dündar Dedekargınoğlu, Yiğit Oskay, Didem Fatma Demir, Samuel Shari Gamaniel, Humayun Ahmed and Aqiq Ishraq for their valuable friendships.

I would like to acknowledge The Scientific and Technological Research Council of Turkey (TÜBİTAK) for supporting this project, under no. 117M434.

I would like to express my sincere gratitude to my family who taught me that education is the most important thing in life and supported me in every way throughout my education life. Without them none of this would have been possible.

Contents

List of Figures

List of Tables

Chapter 1

Introduction

For more than a century, scientists have been conducting various researches to decrease the friction between surfaces to reduce energy loss and prevent wear in surfaces to increase mechanical lifespan, sustainability, and durability. In 1966, Peter Josh and David Tabor presented a report that addressed the needs of the lubrication industry [1]. The authors claimed that an interdisciplinary approach is necessary to study lubrication, wear, friction and introduced the word tribology [1] a field of technology and science that focuses on interacting surfaces in relative motion to study these phenomena. By 2017, approximately 23 % of the world's energy consumption comes from tribological contacts [2]. Given the advances in tribology, worldwide energy losses due to wear and friction may be decreased by 40 % in the following 15 years [2].

For this reason, lubrication takes a critical role in mechanical systems, first to reduce stress generated at the contact boundary to prevent mechanical breakdown and second to reduce energy loss due to friction. Dry surfaces exhibit high friction coefficient due to hardness, waviness, adhesion of the surfaces, and low surface energy, resulting in surface wear. Lubricants are applied to the surface to reduce the friction coefficient and prevent wear. Two types of lubrication are available; solid lubrication and fluid lubrication. In solid lubrication, a thin solid film or a powder form is used between surfaces [3]. Liquid lubrication may appear

in either gaseous or liquid form. For fluid film lubrication, different operating regimes are available. Each of them requires a different mathematical approach to understand its nature. In hydrostatic lubrication, lubricant is transmitted to two surfaces in relative motion by an externally pressurized system [4]. In hydrodynamic lubrication, the hydrodynamic load is provided to a thin film in between surfaces without using external pressure system [5]. If the pressure values are high enough in hydrodynamic lubrication, elastic deformation may occur on the surfaces. This situation causes the characteristic properties of the thin film to change further and the lubrication to switch to a different lubrication regime, elastohydrodynamic lubrication. The term mixed lubrication is referred to the transition region in between hydrodynamic and elastohydrodynamic lubrication [3]. Finally, boundary lubrication is used to describe lubrication where molecular interaction between surfaces is significant because surfaces are very close to each other.

1.1 Mathematical analyses of hydrodynamic lubrication

One of the typical uses of hydrodynamic lubrication is in bearings such as journal bearings, linear pad bearings, surface textured bearings, and squeeze film dampers. In bearings, if the surfaces move fast enough, they can increase the pressure of the lubricant thin film and form enough load to separate the surfaces from each other. To understand how much load the lubricant film can support and the magnitude of the friction force on the surfaces, the film's pressure, density, and velocity fields need to be acquired. Therefore, the mathematical analysis of thin film begins with the solution of full Navier-Stokes equations. However, the solution of the Navier-Stokes equations is numerically difficult, so various assumptions have been made. A well-known Reynolds Equation is used for thin-film approximation, and various solution techniques are available. However, even the Reynolds equation alone is not sufficient to describe all the characteristics of a thin film of a bearing. Different phenomena can change the hydrodynamic

structure of the lubricant in various ways and cause the results to be very different from the conventional solution of the Reynolds equation. In this study, especially two of these phenomena, boundary slippage and cavitation, will be examined. Their physical effects will be merged with the Reynolds equation to provide an accurate mathematical model for hydrodynamic lubrication. Miscellaneous mathematical models are available in the literature to simulate the effects of these two phenomena. Each modeling has its advantages and disadvantages. A literature review was conducted to choose suitable models for the cavitation and the wall slip. The following section will give a literature review.

1.2 Literature review on wall slip boundary condition

One of the conditions from which the classical Reynolds equation is derived is the no-slip boundary condition. In a no-slip boundary condition, the fluid layer adjacent to the surface is assumed to be stationary relative to the motion of the surface. However, experimental results have shown that the widely-adopted no-slip boundary condition, which is valid for macro-scale problems, may fail to predict the hydrodynamic characteristics of flows on hydrophobic surfaces at micro-scale cases. Various experimental studies have been performed to set forth the importance of wall-slip.

Churaev, Sobolev, and Somov had quantified the slip length, a parameter that controls the slip velocity, in thin quartz capillaries using mercury and water in lyophobic capillaries [6]. Furthermore, they found a negative correlation between slippage of water and a rise in the temperature. Vinogradova showed that the water between hydrophobic surfaces exhibits significantly different properties than conventional results [7]. The slippage mechanism explains these differences in thin-film drainage. Pit et al. showed that wall slip is possible with simple Newtonian fluids using the total internal reflection fluorescence recovery after photobleaching technique (TIR-FRAP) by probing the velocity at the wall [8],

and later with hexadecane [9]. Zhu et al. performed experiments using vibrated molecularly smooth surfaces and found that partial slip is possible when the flow rate exceeds a critical level [10]. Furthermore, the limits of boundary slippage are tested, and a transitionary point at surface roughness is reported [11]. It has been showed by [12] and [13] that polymer melts can slip on surfaces. All of these experiments led to the conclusion that boundary slippage may occur depending on the conditions.

Various numerical models have been proposed to simulate boundary slippage. The literature frequently adopts three major approaches: the Navier slip length model, Tresca slip model (critical shear stress model), and modified slip length model (Navier slip length model that incorporates the critical shear stress criterion).

1.2.1 Navier slip length model

The first one is the Navier slip length model, in which the slip velocity of the fluid layer adjacent to the surface is equal to the shear rate of the fluid times a proportionality constant, slip length. For Newtonian fluids, experimental fitting is performed to obtain slip length constant, see [8], [9]. This approach requires a modification on the Reynolds equation. First, the Reynolds equation must be rearranged for the wall slip boundary condition, and later, the slip velocity terms must expand with respect to shear rate and slip length. In this model, regardless of the magnitude of shear stress on the wall, boundary slippage occurs at every point.

A one-dimensional single-textured bearing with Navier slip condition is studied to investigate the effect on load with cavitation in [14]. It has been found out that the only inlet region of the bearing requires a slip zone for optimal load performance. The authors reported that there is a contradictory relationship between hydrodynamic load and friction [14].

Fortier and Salant used Navier slip condition to study two-dimensional engineered slip, no-slip surfaces on plane sliders and showed significant gains of hydrodynamic load could be achieved even in parallel cases [15]. Conventional no-slip boundary condition predicts no-load support at all. The authors extended research to journal bearings with Reynolds condition to simulate cavitation and wall slip simultaneously [16].

1.2.2 Tresca slip model

One of the drawbacks of the Navier slip model is that the boundary slippage is not limited to any specific condition and thus where on the surface it occurs, it is arbitrary. Spikes and Granick claimed that slippage would not occur until shear stress on the wall reaches a critical value [17]. In the Tresca model, shear stress is limited to critical shear stress and cannot exceed this value. Once the shear stress reaches this limit at any point, slippage starts to occur. In this way, wall slip can be limited to some surface parts.

Spikes developed a set of equations to study wall slip at infinitely long and finite half-wetted linear pad bearings [18], and half-wetted journal bearings with Reynolds condition [19]. Significant gains in load on half-wetted bearings (i.e., only one of the wall surfaces is allowed to exhibit boundary slippage) are reported.

Strozzi et al. developed a mathematical model for tangential wall slip problem [20]. Tresca slip model is employed, and variational inequalities are used to model the critical shear stress criterion. The analysis is limited to a one-dimensional linear slider bearing.

A one-dimensional boundary slippage algorithm that accounts for the mass flow conserving cavitation is proposed by Bayada [21]. A compressibility model is used to account for the properties of the cavitation region, a homogeneous liquid-vapor mixture.

Biancofiore et al. used linear complementary variables to couple boundary slippage in one-dimensional lubricated contacts with mass conserving LCP cavitation model [22]. A half-implicit solution algorithm is developed to couple cavitation and slip models. The effect of surface texturing on lubrication performance is investigated.

C.W. Wu et al. studied hydrodynamic lubrication of one-dimensional journal bearings with the presence of wall slip [23]. The effect of the critical shear stress on hydrodynamic characteristics of lubrication film is investigated. Reynolds condition is used to simulate cavitation.

G. J. Ma et al. developed a multi-linearity algorithm for wall slip in two-dimensional gap flows [24]. The equations describing the relationship of wall slip and shear stress are divided into N number o control equations. These equations are solved to obtain the magnitude of slip velocity in predetermined angles. A certain number of directions are needed to reach the desired accuracy. A quadratic programming algorithm is used to solve these coupled equations. This model has also been extended to journal bearings using Reynolds boundary condition to include effects of cavitation [25]. Using the same model, they performed heterogeneous slip/no-slip surface optimization on two-dimensional slider bearings, and parallel gaps [26].

1.2.3 Modified slip length model

A modified slip model that incorporates critical shear stress criterion into Navier slip model is proposed by [17]. Slippage will not start in this model until shear stress reaches critical shear stress. Once the shear stress reaches a critical value, slip occurs with a constant shear rate. This critical shear stress value is not a limit as in the Tresca model but rather an onset value. Bayada studied this model in one-dimensional bearings with mass conserving cavitation model [21].

1.3 Literature review on hydrodynamic cavitation

Cavitation is a phenomenon in which sudden pressure changes in lubricant film cause the formation and collapse of gaseous cavities. Due to the hydrodynamic characteristics of lubricant films, such rapid changes may appear in bearing and alter the pressure and density fields.

Various experiments have been conducted to understand the nature of cavitation. In 1956, Cole and Hughes did experiments on transparent glass journal bearings and photographed the cavitation in film [27]. Zeidan and Vance performed experimenters on squeeze film dampers to identify cavitation zones and their effects on pressure distribution [28]. Braun and Hendricks investigated vaporous/gaseous cavities in eccentric journal bearings [29] and a comparison of experimental results with numerical models is given. Sun et al. did simultaneous measurements with high-speed photography in dynamically loaded journal bearings submerged in the liquid lubricant [30]. Diaz and San Andres compared experimental and theoretical results in open-end squeeze film dampers to analyze homogeneous bubbly mixtures [31]. Experimental and theoretical results of finite submerged squeeze film damper bearings discussed by Ku and Tichy [32].

The presence of cavitation can be seen in the numerical solution of the classical Reynolds equation. The complete Sommerfeld solution showed that a sudden pressure drop follows the pressure rise in converging-diverging geometric profiles, and pressure can decrease to negative values. Therefore, the classical Reynolds equation cannot accurately predict the pressure values in the cavitation region. Further modifications on Reynolds Equation are necessary to ensure cavitation effects are appropriately simulated.

The simplest way of doing it is to assume zero pressure value in possible cavitation region suggested by Gümbel [33]. However, this condition completely ignores the reformation of the cavitation. Another widely adopted condition is the Reynolds condition. The pressure derivatives in the cavitation region are

forced to be zero; however, this condition lacks the reformation of liquid film and hence not mass conserving.

The Jakobsson−Floberg−Olsson (JFO) cavitation model [34], [35] develops unique boundary conditions for both film formation and reformation, which allows the cavitation location within the lubricating film to be simulated more accurately.

Elrond used Jakobsson−Floberg−Olsson cavitation theory [36] and proposed a modified Reynolds equation to solve hydrodynamic lubrication problems numerically. A switch function is appointed to detect the formation and reformation of the cavitation region. This pioneering approach is known as Elrond-Adams model [37].

Bayada and Chambat investigated the free boundary problem in lubrication to predict cavitation location accurately [38]. Bayada and Chupin developed a fully compressible cavitation model that is based on isotropic phase change assumption [39]. The nonlinear relationship between density and pressure is separated into liquid, vapor, and homogeneous two-phase mixture regions. According to the pressure values, the proper relation is used to solve the compressible Reynolds equation. A linear approximation of this compressibility model is implemented into the Reynolds equation and solved with finite difference method by Bayada [40].

A mass conserving complementary formulation to study lubricant films with cavitation is presented by Giacopini et al. [41]. Complementary variables modify the compressible Reynolds equation into a form in which the complementary relations define the cavitation region. Then this modified Reynolds equation is solved through variational inequalities. This model is extended to two-dimensional cases [42].

Woloszynski et al. developed an efficient numerical algorithm for cavitation in hydrodynamic lubrication [43]. The complementary constraints that define active and nonactive regions are reformulated into a continuous differentiable equation.

This equation is solved with the Reynolds equation to obtain pressure and density fields of lubricant films. The algorithm is efficient compared to other widely-used cavitation models in the literature.

A generalized Reynolds equation that accommodates a switch function-based cavitation algorithm for arbitrary compressibility models is presented by Sahlin et al. [44]. It has been reported that the pressure density laws are very sensitive to hydrodynamic load support.

Rayleigh-Plesset equation is used to analyze cavitating bubbles in various types of machinery [45],[46]. Transient evolution of the cavitating bubble (i.e., formation, growth, and collapse) is evaluated considering contributions of cavitation pressure, non-condensable gas, the constant mass of gas assumption, and dynamic viscosity effects [47].

In lubricant films, cavitation does not exist alone. It is often accompanied by other phenomena such as elastic deformation on boundaries, piezoviscous effects, non-Newtonian additives, and viscoelastic effects. Gamaniel et al. studied viscoelastic effects on the performance of lubricated contacts with the presence of cavitation [48]. Elastohydrodynamic lubrication is studied with cavitation, compressibility, and thermal effects in rolling bear elements using finite volume solver by Hajishafiee et al. [49].

1.4 Thesis Layout

This thesis is organized in the following fashion. In chapter 2, a brief derivation of the Reynolds equation and geometrical description of a bearing will take place. Mass conserving LCP model [42] will be used to simulate cavitation. There are two main reasons for choosing this model. First, it can achieve accurate results in samples such as squeeze film dampers as it provides mass conservation. The second reason is that it works robustly under challenging geometries such as micro texture pockets. The multi-linearity algorithm [24], which is based on the Tresca

criterion and therefore proven by experiments, will be used for the boundary slippage. Finally, a multi-linearity wall slip model modification will be presented to create a novel wall slip algorithm. In chapter 3, numerical implementations of equations for finite element method and description of numerical solver will be given. Numerical validation of models will take place in chapter 4. First of all, it will be proven that the LCP mass-conserving cavitation model and multi-linearity wall slip models work accurately together in an explicitly coupled fashion. Later, the speed and accuracy of the new wall slip model presented in this paper will be tested. Finally, in chapter 5 conclusion and future perspectives will be discussed.

Chapter 2

Mathematical model

To study the hydrodynamic characteristics of a bearing requires pressure and shear stress profiles. These profiles can be obtained by solving Navier-Stokes equations. However, solving Navier-Stokes equations with other phenomena such as hydrodynamic cavitation and boundary slippage is challenging numerical-wise. This section will model the approximation of the Naiver-Stokes equation, namely Reynolds Equation, cavitation, and boundary slippage equations.

Before moving on to the detailed models, a numerical difficulty must be addressed. Slip velocity profiles of the bearing are required to solve the cavitation problem, and the pressure profiles obtained by solving the cavitation problem are required to solve the boundary slippage problem. Therefore the two problems and the equations expressing them are coupled. In this study, when solving cavitation and boundary slippage phenomena, it is assumed that the required profiles (slip velocity and pressure, receptively) are known prior. Then, using an explicit iterative algorithm, these profiles will be updated, and finally, correct profiles will be acquired.

2.1 The Reynolds equation

Solution of the full Navier-Stokes equations are numerically challenging; therefore, miscellaneous simplifications are available in the literature. A well-known approximation for lubricants in thin films is made by Osborne Reynolds [50]. Full Navier-Stokes equations can be simplified to Reynolds equation under the following assumptions:

1. The continuum description is valid.
2. The Navier-Stokes equations hold.
3. The film is thin.
4. The flow is laminar.
5. The lubricant is Newtonian.

The detailed derivations of Reynolds Equation are available through literature, see [51]; therefore, a brief derivation is given below. Thin-film approximation introduces significant differences in the order of magnitude of pressure derivatives in the film; therefore, the pressure derivative across film height (z-axis, see figure 2.1) can be ignored. Taking into account other assumptions the x and y momentum equations become,

$$\frac{\partial p}{\partial x} = \frac{\partial}{\partial z}(\mu \frac{\partial u}{\partial z}) \tag{2.1}$$

$$\frac{\partial p}{\partial y} = \frac{\partial}{\partial z}(\mu \frac{\partial v}{\partial z}) \tag{2.2}$$

where u and v denote the velocity components of the velocity vector of the x and the y axis, respectively, and μ represents the lubricant's viscosity. Integrating equation (2.1) and (2.2) along z-axis yields to velocity fields.

$$u = \frac{1}{2}\frac{\partial p}{\partial x} z^2 + Az + B \tag{2.3}$$

$$v = \frac{1}{2}\frac{\partial p}{\partial y} z^2 + Cz + D \tag{2.4}$$

Integration constant of equation (2.3) and (2.4) can be obtained by applying following boundary conditions.

$$\begin{aligned} u = U_a, \quad v = V_a, \quad at \quad z = 0 \\ u = U_b, \quad v = V_b, \quad at \quad z = h \end{aligned} \tag{2.5}$$

Using continuity equation for mass conservation,

$$\frac{\partial \rho}{\partial t} + \frac{\partial u}{\partial x} + \frac{\partial y}{\partial y} + \frac{\partial w}{\partial z} = 0 \tag{2.6}$$

the two-dimensional unsteady compressible Reynolds Equation is obtained.

$$\frac{\partial}{\partial x}(\frac{h^3}{6\mu}\rho\frac{\partial p}{\partial x}) + \frac{\partial}{\partial y}(\frac{h^3}{6\mu}\rho\frac{\partial p}{\partial y}) = \frac{\partial(\rho h(U_a + U_b))}{\partial x} + \frac{\partial(\rho h(V_a + V_b))}{\partial y} + 2\frac{\partial(\rho h)}{\partial t} \tag{2.7}$$

Once the equation (2.7) is solved, pressure and density fields of a bearing for any arbitrary geometry and viscosity can be obtained.

2.2 Geometrical description of a bearing

Before defining the cavitation model and control equations for the boundary slippage, it is necessary to address the bearings' geometric structure and some boundary conditions. The following limitations are used for all bearings to be modeled and sample problems to be solved in this study. It is assumed that the bottom surface of the bearing is sliding with constant velocity U and the top surface is stationary. Furthermore, it is assumed that the slippage can only occur on the top surface. The circumference of the bearing is considered to be open to the atmosphere; therefore, a constant pressure p_a is appointed for boundary conditions. Velocities u_s and v_s are used to define the slip velocities of the top surface on the x and the y-axis, respectively. The Reynolds equation is modified considering the slip velocities on the top surface, aforementioned geometrical parameters, and boundary conditions.

$$\frac{\partial}{\partial x}(\frac{h^3}{6\mu}\rho\frac{\partial p}{\partial x}) + \frac{\partial}{\partial y}(\frac{h^3}{6\mu}\rho\frac{\partial p}{\partial y}) = \frac{\partial(\rho h(U + u_s))}{\partial x} + \frac{\partial(\rho h(v_s))}{\partial y} + 2\frac{\partial(\rho h)}{\partial t} \tag{2.8}$$

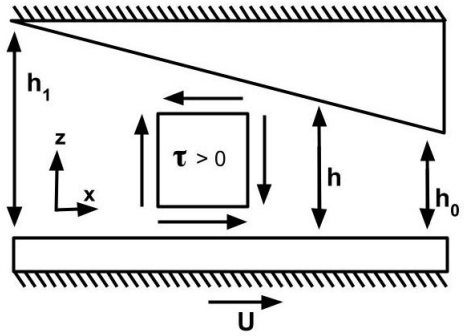

Figure 2.1: The model for the slider bearing.

2.3 Hydrodynamic cavitation

In this research, the cavitation model will be based on a mass conserving complementary formulation [41].

2.3.1 Complementarity formulation

The complementarity formulation is achieved by first defining the complementary variables and determining the functional relationship between those variables. There exist two regions in film separated by the presence of the cavitation. In the full film region (active region), the film's pressure and density are greater than cavitation pressure and saturation density, respectively; therefore, the film is liquid. In the cavitation region (nonactive region), the pressure and density of the film are lower than cavitation pressure and saturation density, respectively. This situation yields cavities within the film, which are a liquid-vapor mixture. These observations indicate that the film's structure is controlled by pressure and density. Some adjustments will be made to pressure and density before choosing complementary variables. First of all, the pressure is rescaled according to the cavitation pressure $(P - P_c)$; thus, if the pressure drops to zero, cavitation will occur. In this case, the presence of cavitation will depend on whether the pressure is greater than 0 or not. Secondly, a normalized density (void fraction)

r is introduced by,

$$r = 1 - \frac{\rho}{f(p)\rho_c} \tag{2.9}$$

where $f(p)$ is the functional relationship between density and pressure in the active region and ρ_c is the density at saturation point. If there is no cavitation, then the r is always zero. If cavitation occurs, it will take a value greater than zero. After these modifications, the following situation is revealed. If there is no cavitation (the whole film is liquid), then p > 0 and r = 0, else cavitation occurs within the film and p = 0 and r > 0. Pressure and void fraction are suitable complementary variables to control the presence of cavitation. The functional relationship between pressure and void fraction inequalities becomes,

$$p \geq 0, \tag{2.10a}$$

$$r \geq 0, \tag{2.10b}$$

$$p \cdot r = 0 \tag{2.10c}$$

These functional relationships are valid throughout the entire film. Reynolds equation will be adjusted to these complementary variables. Using equation (2.8) and (2.9), Reynolds Equation can be rewritten as follow,

$$\frac{\partial}{\partial x}(\frac{h^3}{6\mu}(1-r)f(p)\rho_c\frac{\partial p}{\partial x}) + \frac{\partial}{\partial y}(\frac{h^3}{6\mu}(1-r)f(p)\rho_c\frac{\partial p}{\partial y}) = \frac{\partial((1-r)f(p)\rho_c h(U+u_s))}{\partial x} + \frac{\partial((1-r)f(p)\rho_c h(v_s))}{\partial y} + 2\frac{\partial((1-r)f(p)\rho_c h)}{\partial t} \tag{2.11}$$

Expanding the derivatives and dividing both sides by ρ_c results in,

$$\frac{\partial}{\partial x}(\frac{h^3}{6\mu}f(p)\frac{\partial p}{\partial x}) - \frac{\partial}{\partial x}(\frac{h^3}{6\mu}rf(p)\frac{\partial p}{\partial x}) + \frac{\partial}{\partial y}(\frac{h^3}{6\mu}f(p)\frac{\partial p}{\partial y}) - \frac{\partial}{\partial y}(\frac{h^3}{6\mu}rf(p)\frac{\partial p}{\partial y}) = + \frac{\partial}{\partial x}(f(p)h(U+u_s)) - \frac{\partial}{\partial x}(f(p)rh(U+u_s)) + \frac{\partial}{\partial y}(f(p)hv_s) - \frac{\partial}{\partial y}(f(p)rhv_s) + 2\frac{\partial(f(p)h)}{\partial t} - 2\frac{\partial(f(p)rh)}{\partial t} \tag{2.12}$$

Two issues has to be addressed in equation (2.12). In active region r takes zero value, and in non-active region pressure is constant, and its derivative is zero, therefore $\frac{\partial p}{\partial x} \cdot r$ is always zero in the film despite the region. Furthermore, in non-active region $f(p) = 1$ meanwhile in active region r=0, therefore the terms

containing $f(p) \cdot r$ can be simplified to r. The modifications mentioned above lead to the final form of the Reynolds equation.

$$\begin{aligned} &\frac{\partial}{\partial x}(f(p)\frac{h^3}{6\mu}\frac{\partial p}{\partial x}) + \frac{\partial}{\partial y}(f(p)\frac{h^3}{6\mu}\frac{\partial p}{\partial y}) - \frac{\partial}{\partial x}(f(p)h(U+u_s)) - \frac{\partial}{\partial y}(f(p)hv_s) \\ &+ \frac{\partial}{\partial x}(rh(U+u_s)) + \frac{\partial}{\partial y}(rhv_s) - 2\frac{\partial(f(p)h)}{\partial t} + 2\frac{\partial(rh)}{\partial t} = 0 \end{aligned} \tag{2.13}$$

Equation (2.13) will be solved with the functional relationships of (2.10) in order to obtain the pressure and void fraction (therefore density) fields of any bearing.

2.4 Boundary slippage

In a one-directional problem, wall slip can occur only either downstream or upstream; therefore, it is easy to find the direction of the slippage. However, in the two-dimensional problem, both angle and magnitude of the slip vector are uncertain. For this reason, a unique solution method is required to calculate the direction and magnitude simultaneously. In this research, an alternative version of the multi-linearity algorithm for wall slip [24] is used. Before defining the boundary slippage method, it is necessary to define the control equations of the shear stresses and slip velocities on the surfaces.

2.4.1 Control equations

The shear stress components of the fluid layer adjacent to the top surface of the bearing on the x and y-axis can be written as,

$$\tau_{xz} = -\frac{h}{2}\frac{\partial p}{\partial x} + (U - u_s)\frac{\mu}{h} \tag{2.14a}$$

$$\tau_{yz} = -\frac{h}{2}\frac{\partial p}{\partial y} + (-v_s)\frac{\mu}{h} \tag{2.14b}$$

For the details of the derivation of the equation (2.14), see [20]. The individual slip velocities on the x and y-axis, u_s and v_s can be rewritten as,

$$u_s = \lambda \cdot cos\beta \tag{2.15a}$$

$$v_s = \lambda \cdot sin\beta \tag{2.15b}$$

where λ is the slip velocity magnitude and the β is the angle between the slip vector and the positive x axis, see figure 2.2.

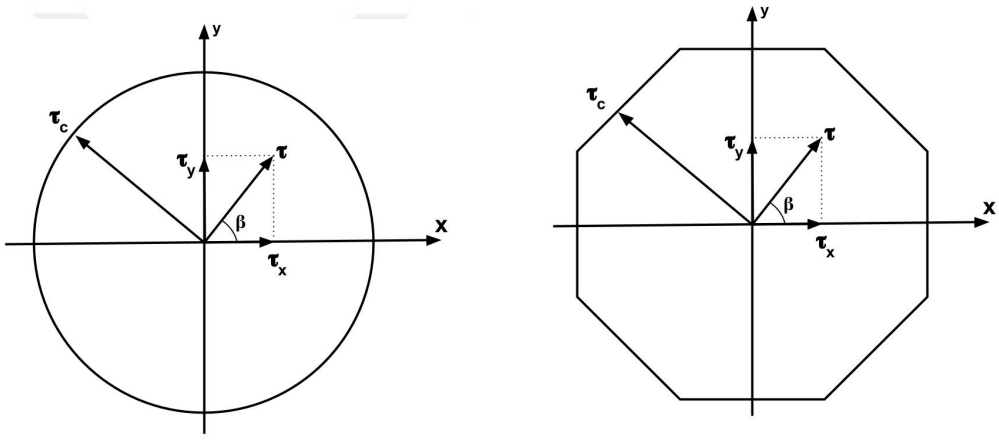

(a) Shear stress and its limit.

(b) 8-Directional approximation of shear stress and its limit.

Figure 2.2: Tresca model for boundary slippage, (a) Shear stress and its limit, (b) 8-Directional approximation of shear stress and its limit.

It should be noted here that, the shear stress at the interface always opposes the slip velocity and therefore, the signs of shear stress and slip velocity should always be opposite of each other. In this configuration, shear stress on the interface is defined with negative sign with respect to x-axis and slip velocity with positive sign, see figure 2.1. It is possible to use the opposite signs and it will indicate the same physical condition. For a more detailed explanation, see [18]. The shear stress vector becomes,

$$\boldsymbol{\tau} = \tau_{xz}\mathbf{1} + \tau_{yz}\mathbf{J} \tag{2.16}$$

and the magnitude of the shear stress vector is,

$$\tau = \sqrt{\tau_{xz}^2 + \tau_{yz}^2} \tag{2.17}$$

Replacing equation (2.14) and (2.15) into (2.17) results in,

$$\tau^2 = (-\frac{h}{2}\frac{\partial p}{\partial x} + (U - \lambda \cdot cos\beta)\frac{\mu}{h})^2 + (-\frac{h}{2}\frac{\partial p}{\partial y} + (-\lambda \cdot sin\beta)\frac{\mu}{h})^2 \tag{2.18}$$

Equation (2.18) which defines the relationship between shear stress and slip velocity on the interface, contains nonlinear variables of τ^2 and λ^2 and therefore, the solution is numerically tricky. The projection of the shear stress vector onto the x and y axes will be used to avoid nonlinear variables instead of the magnitude of the shear stress vector itself.

$$\tau_{xz} = \tau \cdot cos(\beta) \tag{2.19a}$$

$$\tau_{yz} = \tau \cdot sin(\beta) \tag{2.19b}$$

An alternative way of expressing shear stress can be obtained by multiply equation (2.19a) and (2.19b) by $cos(\beta)$ and $sin(\beta)$ respectively and summing them.

$$\tau = \tau_{xz} \cdot cos(\beta) + \tau_{yz} \cdot sin(\beta) \tag{2.20}$$

Placing euqation (2.14) and (2.15) into (2.20) results in,

$$\tau = (-\frac{h}{2}\frac{\partial p}{\partial x} + (U - \lambda \cdot cos\beta)\frac{\mu}{h}) \cdot cos(\beta) + (-\frac{h}{2}\frac{\partial p}{\partial y} + (-\lambda \cdot sin\beta)\frac{\mu}{h}) \cdot sin(\beta) \tag{2.21}$$

Equation (2.21) contains only linear variables of τ and λ therefore easier to solve numerically.

2.4.2 Complementarity formulation for fixed N-direction boundary slippage problem

The Tresca model describes the tangential slip relationship between the adjacent fluid layer and the solid interface. If the shear stress on the interface τ is less than a constant limit, namely critical shear stress τ_c, then no slip occurs, and λ is zero. If the shear stress τ, reaches τ_c, then shear stress cannot be greater than τ_c and slip occurs with non zero λ. Because of this situation $(\tau - \tau_c) \cdot \lambda$ is always zero throughout the surface. Based on the above observations, it can be concluded that the shear stress and the slip velocity control the boundary slippage on the surface; thus, the complementary variables of equation (2.21) are λ and τ. With the rearrangement of equation (2.21) the slip problem can be expressed as,

$$\tau = -\frac{h}{2}(\frac{\partial p}{\partial x}cos\beta + \frac{\partial p}{\partial y}sin\beta) - \lambda\frac{\mu}{h}(cos(\beta) + sin(\beta)) + U\frac{\mu}{h}cos\beta \tag{2.22a}$$

$$\lambda \geq 0 \tag{2.22b}$$

$$\tau_c - \tau \geq 0 \tag{2.22c}$$

$$(\tau - \tau_c) \cdot \lambda = 0 \tag{2.22d}$$

When the above system is solved, shear stress and slip velocity fields on the surface can be calculated. Without proceeding further, it will be assumed that the correct pressure and pressure derivatives corresponding to slip velocities are known. This conjecture will be handled later using an explicit algorithm, and details will be given in the next sections. Equation (2.22a) cannot be solved with functional relations of (2.22b), (2.22c) and (2.22d) because it contains one more unknown, the slippage angle β. This situation arises on a two-dimensional problem because both the angle and magnitude of the slip are a priori unknown. In one-dimensional problems, the direction of the slip is either downstream or upstream; however, in the two-dimensional slip problem, there are infinite numbers of possible slip angles. Multi-linearity algorithm [24] is used to overcome this challenge. In the multi-linearity algorithm, a discrete number of angles at which the slip will occur are predetermined, and equation (2.20) is discretized into N number of control equations, see figure 2.2b. In this way, the angles in which slip can occur are limited, and the previously undetermined slip angle is eliminated. The surface shear stress for each slip direction becomes,

$$\tau^D = \tau_{xz} \cdot cos(\beta^D) + \tau_{yz} \cdot sin(\beta^D) \quad for \quad D = 1, 2, ..., N \tag{2.23}$$

where,

$$\beta^D = \frac{2\pi}{N}(D-1) \quad for \quad D = 1, 2, ..., N \tag{2.24}$$

The subscript D is used to indicate the direction number. There is a unique λ and τ for each direction, and therefore the total number of complementary variables is two times the number of directions. The slip velocities in the x and y direction can be expressed as the summation of the individual slip velocities in each direction.

$$u_s = \sum_D^N \lambda^D \cdot cos(\beta^D) \tag{2.25a}$$

$$v_s = \sum_D^N \lambda^D \cdot sin(\beta^D) \tag{2.25b}$$

Finally, to simplify the equations, a new complementary variable is introduced.

$$\gamma = \tau_c - \tau \tag{2.26}$$

Using equation (2.23),(2.24),(2.25),(2.26) and (2.14), final slip control equations are obtained.

$$\begin{aligned}\gamma^D =& \frac{h}{2}\left(\frac{\partial p}{\partial x}cos(\beta^D) + \frac{\partial p}{\partial y}sin(\beta^D)\right) + U\frac{\mu}{h}cos(\beta^D) + \tau_c \\ &+ \frac{\mu}{h}\left(cos(\beta^D)(\sum_D^N \lambda^D \cdot cos\beta^D) + sin(\beta^D)(\sum_D^N \lambda^D \cdot sin\beta^D)\right)\end{aligned} \tag{2.27}$$

$$\gamma^D \geq 0 \tag{2.28a}$$

$$\lambda^D \geq 0 \tag{2.28b}$$

$$\gamma^D \cdot \lambda^D = 0 \tag{2.28c}$$

Equation (2.27) and functional relations of (2.28) define the relationship between slip velocity and surface shear stress for each predetermined N number of directions and are ready to be solved. Before proceeding on to the improved model proposed in this study, it is helpful to emphasize some of the issues related to this slip model, so it will be clear why a different model is proposed.

To avoid name confusion in this paper, multi-linearity model for wall slip which is proposed by G.J. Ma et al. [24], will be called as fixed N-direction slip model.

First of all, in this boundary slippage algorithm where the control equations are divided to N number of possible slip directions, the actual slip velocity of the system is calculated by summation of the slip velocities in all directions. This value is used to calculate the shear stress in each direction. Thus, the shear stress in each slip direction depends on the N number of velocity variables (this value is 1 in a one-dimensional problem), making the solution matrices complex as the number of directions increase, see equation 3.20.

Another disadvantage is that the critical shear stress limits the projection of the shear stress in each direction, but the actual shear stress may differ from this

value. An example can be given to explain this situation. Suppose that where the surface slip is to occur, the system is divided into 4 different directions where, $\beta^1 = 0$, $\beta^2 = \pi/2$, $\beta^3 = 2\pi/2$ and $\beta^3 = 3\pi/2$. Suppose the projection of the shear stress reaches the critical shear stress in two adjacent directions simultaneously (which is possible by equations), namely directions 1 and 2. In that case, the slip will start in both directions simultaneously, indicating the actual slip angle is $\pi/4$, and the magnitude of actual shear stress of the system is greater than the critical shear stress. This circumstance will cause the shear stress to be limited to a value greater than τ_c, see figure 2.3.

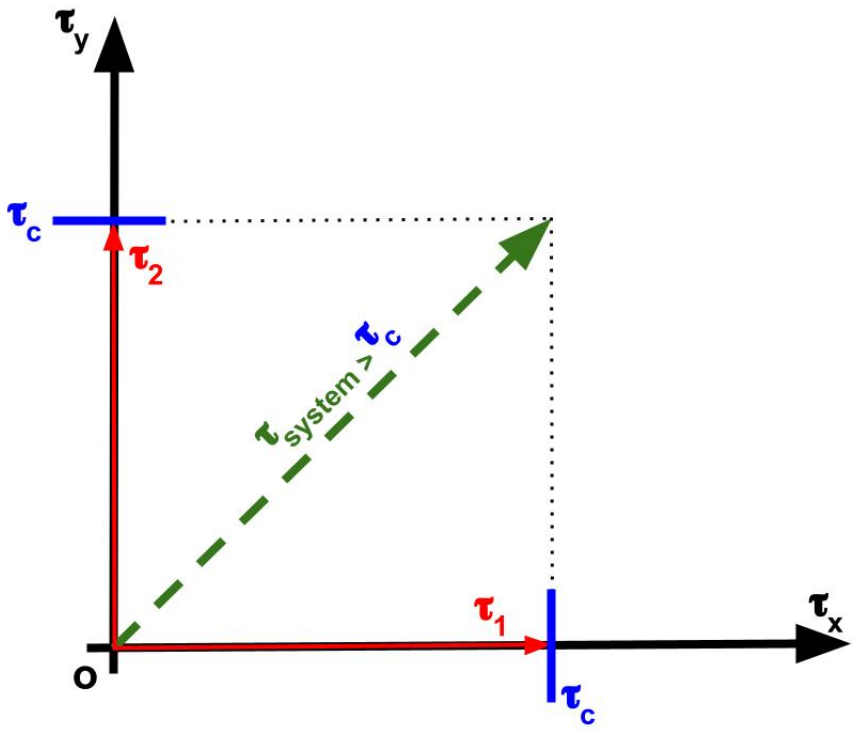

Figure 2.3: Actual shear stress between two adjacent directions, τ_1 and τ_2, fixed 4 direction slip model.

A high number of directions are needed to avoid this situation; for example, N=16 is required for cylindrical pure squeezing motion, which is symmetric for each quadrant, for details see [24]. Using more directions will increase the number of elements in the solution matrices by order of N^2; thus, the solution time required to solve the matrices will increase significantly; therefore, there is a trade-off between accuracy and computational time. Numerical examples for this

case will be given in the following chapters.

In the next section, an improved method for boundary slippage (modifications on multi-linearity slip model), which is more accurate and computationally affordable at the same time, will be proposed.

2.4.3 Complementarity formulation for rotating 3-direction boundary slippage problem

In this new method, the number of possible slip directions is limited to 3. These three directions are separated from each other by $\frac{2\pi}{3}$ degrees, see τ^1, τ^2, and τ^3 in figure 2.4. τ^1 will be the main slip direction and will be used to calculate the shear stress and slip velocity of the system, while the others τ^2 and τ^3 will not be used to calculate slip velocity but will be used to set the angle of the slip, β^1, by rotating the system. In other words here, the two-dimensional slip problem is reduced to one dimension problem (to the direction of τ^1) and tau τ^2 and τ^3 are used to find the correct angle of τ^1. There exists a difference compared to the fixed N-direction method given previously. In the fixed N-direction method, the summation of the velocities in all slip directions is used to calculate the actual slip velocity, while in the rotating 3-direction method, only the slip velocity in direction one will be used. This is because when direction one is changed and aligned with the real slip direction, the velocities in the remaining directions will be zero naturally; therefore, it is sufficient to use only the slip velocity in direction one. The slip velocities of the system in the x and y axes are,

$$u_s = \lambda^1 \cdot cos(\beta^1) \tag{2.29a}$$

$$v_s = \lambda^1 \cdot sin(\beta^1) \tag{2.29b}$$

This formulation enable to use banded matrices in the solution procedure which are relatively easy to deal with, see figure 3.30.

In the first stage of the algorithm, initially, the angle of the slip direction (angle of direction one) is assumed to be zero; second and third directions will be

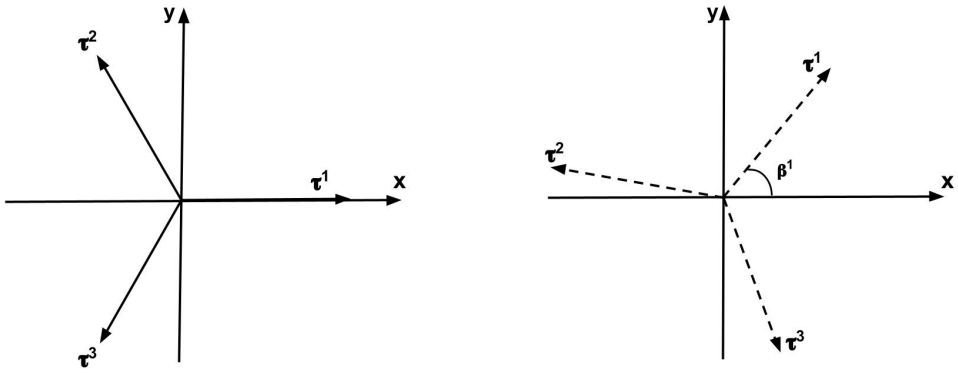

(a) Before rotation. (b) After rotation.

Figure 2.4: Model for rotating three direction slip system, (a) directions before the rotation, (b) directions after the rotation.

separated from it by $\pi/3$ and $2\pi/3$ degrees, see figure 2.4a. Then the equation describing the relationship between shear stress and slip velocity will be solved for this configuration, see equation 2.31; however, this configuration (or in other words β^1) is not correct, and it is assumed. In the second stage, the system will be rotated by β_r to reach the correct configuration. After the solution of the initial configuration,

- If $\tau^2 > \tau^3$ then, the actual slip direction of the system needs to be between directions one and two, and the system is rotated counterclockwise by β_r.
- If $\tau^3 > \tau^2$ then, the actual slip direction of the system needs to be between directions one and three, and the system is rotated clockwise by β_r.
- If $\tau^2 = \tau^3$ and $\tau^1 > 0$ then, the correct slip direction is found.
- If $\tau^2 = \tau^3$ and $\tau^1 < 0$ then, direction one corresponds to the negative part of correct slip direction and is rotated by π degrees to correct.

The second stage of the algorithm is repeated until in all of the nodes $\tau^2 = \tau^3$. Once this condition is reached at all nodes, the correct slip direction is found everywhere, and the simulation is terminated. In the resulting configuration,

β^1 indicates the slip direction, see figure 2.4b. The complementary formulation is slightly different then fixed N-direction slip method because of the difference in equation (2.25) and (2.29). The surface shear stress for each slip direction becomes,

$$\tau^D = \tau_{xz} \cdot cos(\beta^D) + \tau_{yz} \cdot sin(\beta^D) \quad for \quad D = 1, 2, 3 \tag{2.30}$$

Using equation (2.30),(2.24),(2.29),(2.26) and (2.14), final slip control equations are obtained

$$\gamma^D = \frac{h}{2}(\frac{\partial p}{\partial x}cos(\beta^D) + \frac{\partial p}{\partial y}sin(\beta^D)) + \frac{\mu}{h}\lambda^D - U\frac{\mu}{h}cos(\beta^D) + \tau_c \tag{2.31}$$

with complementary relations of,

$$\gamma^D \geq 0 \tag{2.32a}$$

$$\lambda^D \geq 0 \tag{2.32b}$$

$$\gamma^D \cdot \lambda^D = 0 \tag{2.32c}$$

A method has been proposed to calculate the rotation angle (β_r) in each step of the solution to decrease the number of total rotations and increase the algorithm's computational speed. First, a numerical residual is defined to check whether the correct slip angle is found or not.

$$R = |1 - \frac{\gamma_2}{\gamma_3}| \tag{2.33}$$

Then this residual is multiplied by a constant angle to find the rotation angle β_r.

$$\beta_r = R \cdot \beta_c \tag{2.34}$$

where,

$$\frac{\pi}{36} < \beta_c < \frac{\pi}{18} \tag{2.35}$$

Value of β_c has been found by numerical simulations for the optimum speed. To avoid name confusion, modified multi-linearity model for wall slip which is proposed in this paper, will be called as rotating 3-direction slip model.

2.5 Liquid compressibility

The functional correction between pressure and density is represented by parameter f(p) to account for the compressibility of a liquid. For an incompressible liquid, the following relationship is used,

$$f(p) = 1 \tag{2.36}$$

therefore, has no effect on the equation (2.13). Various expressions are available in the literature for a compressible liquid to describe this functional relationship. In this study, an accurate model which is based on experimental results proposed by Downson and Higginson [52] is used to simulate liquid compressibility.

$$f(p) = \frac{C_1 + C_2 \cdot p}{C_1 + p} \tag{2.37}$$

where $C_1 = 0.59 \cdot 10^9$ and $C_2 = 1.34$ is used. Any other baratropic compressbility relationship is easily applicable to this model.

Chapter 3

Numerical implementations

In this chapter the algorithm and the numerical methods for the pressure-density equation (2.13) and shear stress-slip velocity equation (2.31) will be given. Equation (2.13) depends on the slip velocities and equation (2.31) depends on pressure derivatives therefore, they are coupled. In this case, to solve these two equations and their complementary variables, namely, pressure, shear stress, normalized density, and slip velocities, these two equations should be solved simultaneously, and the four unknown variables should be calculated simultaneously. However, this approach introduces a numerical difficulty because combining the complementary variables and equations in a single matrix introduces non-linear complementary variables. In order to eliminate this difficulty, these two equations will be separated from each other and solved in an explicit way. A similar approach for one-dimensional domain had been studied in [22] and this method will be applied to a two-dimensional domain in this work.

3.1 Numerical method for cavitation problem

Finite element method, Galerkin method, is implemented to solve the equation (2.13) with complementary variables of (2.10). The same method in [42] is followed with slight modifications. Assuming a general test function W, equation (2.13) is first multiplied by it and then integrated over the entire domain.

$$\int_\Omega W\Big[\frac{\partial}{\partial x}(f(p)\frac{h^3}{6\mu}\frac{\partial p}{\partial x})+\frac{\partial}{\partial y}(f(p)\frac{h^3}{6\mu}\frac{\partial p}{\partial y})-\frac{\partial}{\partial x}(f(p)h(U+u_s))-\frac{\partial}{\partial y}(f(p)hv_s) + \frac{\partial}{\partial x}(rh(U+u_s))+\frac{\partial}{\partial y}(rhv_s)-2\frac{\partial(f(p)h)}{\partial t}+2\frac{\partial(rh)}{\partial t}\Big]d\Omega=0 \tag{3.1}$$

Separation of individual terms result in,

$$\begin{aligned}&\int_\Omega W\frac{\partial}{\partial x}(f(p)\frac{h^3}{6\mu}\frac{\partial p}{\partial x})d\Omega+\int_\Omega W\frac{\partial}{\partial y}(f(p)\frac{h^3}{6\mu}\frac{\partial p}{\partial y})d\Omega-\int_\Omega W\frac{\partial}{\partial x}(f(p)h(U+u_s))d\Omega\\&-\int_\Omega W\frac{\partial}{\partial y}(f(p)hv_s)d\Omega+\int_\Omega W\frac{\partial}{\partial x}(rh(U+u_s))d\Omega+\int_\Omega W\frac{\partial}{\partial y}(rhv_s)d\Omega\\&-\int_\Omega W2\frac{\partial(f(p)h)}{\partial t}d\Omega+\int_\Omega W2\frac{\partial(rh)}{\partial t}d\Omega=0\end{aligned} \tag{3.2}$$

The first two terms of the equation (3.2) can be simplified further by divergence theorem, and hence the order of the differential equations reduces.

$$\int_\Omega W\frac{\partial}{\partial x}(f(p)\frac{h^3}{6\mu}\frac{\partial p}{\partial x})d\Omega=\int_\Gamma W\left(f(p)\frac{h^3}{6\mu}\frac{\partial p}{\partial x}\right)n_x d\Gamma-\int_\Omega f(p)\frac{h^3}{6\mu}\frac{\partial W}{\partial x}\frac{\partial p}{\partial x}d\Omega \tag{3.3a}$$

$$\int_\Omega W\frac{\partial}{\partial y}(f(p)\frac{h^3}{6\mu}\frac{\partial p}{\partial y})d\Omega=\int_\Gamma W\left(f(p)\frac{h^3}{6\mu}\frac{\partial p}{\partial y}\right)n_y d\Gamma-\int_\Omega f(p)\frac{h^3}{6\mu}\frac{\partial W}{\partial y}\frac{\partial p}{\partial y}d\Omega \tag{3.3b}$$

The first terms of the right-hand side of the equation (3.3) will be evaluated on the domain boundaries; where pressure will be specified; therefore, these terms can be eliminated. Using equation (3.3), the weak form of the equation (3.1) can

be expressed as,

$$
\begin{aligned}
&-\int_\Omega f(p)\frac{h^3}{6\mu}\frac{\partial W}{\partial x}\frac{\partial p}{\partial x}d\Omega-\int_\Omega f(p)\frac{h^3}{6\mu}\frac{\partial W}{\partial y}\frac{\partial p}{\partial y}d\Omega-\int_\Omega W\frac{\partial}{\partial x}(f(p)h(U+u_s))d\Omega\\
&-\int_\Omega W\frac{\partial}{\partial y}(f(p)hv_s)d\Omega+\int_\Omega W\frac{\partial}{\partial x}(rh(U+u_s))d\Omega+\int_\Omega W\frac{\partial}{\partial y}(rhv_s)d\Omega\\
&-\int_\Omega W2\frac{\partial(f(p)h)}{\partial t}d\Omega+\int_\Omega W2\frac{\partial(rh)}{\partial t}d\Omega=0
\end{aligned}
\tag{3.4}
$$

The two-dimensional solution domain is partitioned into a finite number of elements, and equation (3.4) is discretized over each element. The unknown variables of (3.4), p, and r can be interpolated inside each element of the domain with shape functions.

$$p=\sum_{i=1}^{N_n}N_ip_i \tag{3.5a}$$

$$r=\sum_{i=1}^{N_n}N_ir_i \tag{3.5b}$$

where N_n is the number of nodes per element and N_i is the proper shape function. Bilinear shape functions are used for interpolations. For a two dimensional problem, shape functions become,

$$
\begin{aligned}
N_1&=(1-\zeta)(1-\eta)\frac{1}{4}\\
N_2&=(1+\zeta)(1-\eta)\frac{1}{4}\\
N_3&=(1+\zeta)(1+\eta)\frac{1}{4}\\
N_4&=(1-\zeta)(1+\eta)\frac{1}{4}
\end{aligned}
\tag{3.6}
$$

where ζ and η are the local element coordinates. The derivation of interpolation of unknown variables can be expressed as a function of derivatives of shape functions.

$$\frac{\partial p}{\partial x}=\sum_{i=1}^{N_n}\frac{\partial N_i}{\partial x}p_i \tag{3.7a}$$

$$\frac{\partial r}{\partial x}=\sum_{i=1}^{N_n}\frac{\partial N_i}{\partial x}r_i \tag{3.7b}$$

It has been reported by L. Bertocchi et al. in [42] that undesired oscillation may occur in normalized density in the cavitation region because of the hyperbolic

character of the equation (2.13). Therefore a particular case of test functions are investigated by L. Bertocchi et al. Decentered polynomial functions

$$W_i = N_i + \alpha \frac{\partial N_i}{\partial x} sign(U) \tag{3.8}$$

where $\alpha = 0$ is the Galerkin approximation and $\alpha = 1$ is fully up-winded discrete function. An alternative method presented by Luca Bertocchi in which using a particular integration point and its corresponding weight that is equivalent to using upwinded the discrete function is employed here. Integration point m=ξ_{int} and weight $w_m = 2$ where ξ_{int} takes value between 0 and 1 is used to simulate up-winded test functions rather than actually using, for detailed explanation see [42]. The integrals of equation (3.4) is evaluated numerically by Gaussian quadrature rule and discretized on the j'th node of the element Ω_e.

$$\begin{aligned}
F_j(\Omega_e) = &- \sum_{m=1}^{N_{gp}} \Big[\sum_{k=1}^{N_n} \frac{1}{6} \frac{h_m^3 f(p)_m}{\mu_m} \Big(\frac{\partial N_{mk}}{\partial x} p_k \frac{\partial W_{mj}}{\partial x} + \frac{\partial N_{mk}}{\partial y} p_k \frac{\partial W_{mj}}{\partial y} \Big) \Big] w_m \Delta\Omega_m \\
&+ \sum_{m=1}^{N_{gp}} \Big[\sum_{k=1}^{N_n} W_{mj} \Big(\frac{\partial N_{mk}}{\partial x} r_k h_k (U + u_{s,k}) \Big) \Big] w_m \Delta\Omega_m \\
&+ \sum_{m=1}^{N_{gp}} \Big[\sum_{k=1}^{N_n} W_{mj} \Big(\frac{\partial N_{mk}}{\partial y} r_k h_k v_{s,k} \Big) \Big] w_m \Delta\Omega_m \\
&- \sum_{m=1}^{N_{gp}} \Big[W_{mj} \frac{\partial}{\partial x} \Big(f(p)_m h_m (U + u_{s,m}) \Big) \Big] w_m \Delta\Omega_m \\
&- \sum_{m=1}^{N_{gp}} \Big[W_{mj} \frac{\partial}{\partial y} \Big(f(p)_m h_m v_{s,m} \Big) \Big] w_m \Delta\Omega_m \\
&+ \frac{2}{\Delta t} \sum_{m=1}^{N_{gp}} \Big[\sum_{k=1}^{N_n} W_{mj} N_{mk} \Big(r_k(t) h_k(t) - r_k(t - \Delta t) h_k(t - \Delta t) \Big) \Big] w_m \Delta_m \\
&- \frac{2}{\Delta t} \sum_{m=1}^{N_{gp}} \Big[W_{mj} \Big(f(p(t))_m h(t)_m - f(p(t - \Delta t))_m h(t - \Delta t)_m \Big) \Big] w_m \Delta_m \\
&= 0
\end{aligned} \tag{3.9}$$

In equation (3.9) the index m stands for general Gaussian point, w_m is the weight for relevant point, $\Delta\Omega_m$ is the determinant of the coordinate transformation from the global coordinate system to the local element coordinate system. The k index traces the nodes of an element. N_{gp} is the number of Gauss points, and N_n is the

number of nodes per element. There are three different terms in this equation. One of them is the pressure variable multipliers, the other is the normalized density variable multipliers, and the last is free terms. When equation (3.9) is written for each point of the system, it takes the following form.

$$[A]p + [B]r + [C] = 0, \tag{3.10}$$

where

$$A_{j,k} = -\sum_{n=1}^{N_e}\Big\{\sum_{m=1}^{N_{gp}}\Big[\sum_{k=1}^{N_n}\frac{1}{6}\frac{h_m^3 f(p)_m}{\mu_m}\Big(\frac{\partial N_{mk}}{\partial x}\frac{\partial W_{mj}}{\partial x} + \frac{\partial N_{mk}}{\partial y}\frac{\partial W_{mj}}{\partial y}\Big)\Big]w_m\Delta\Omega_m\Big\} \tag{3.11a}$$

$$\begin{aligned} B_{j,k} = &\sum_{n=1}^{N_e}\Big\{\sum_{m=1}^{N_{gp}}\Big[\sum_{k=1}^{N_n}W_{mj}\Big(\frac{\partial N_{mk}}{\partial x}h_k(U+u_{s,k})\Big) + \sum_{k=1}^{N_n}W_{mj}\Big(\frac{\partial N_{mk}}{\partial y}h_k v_{s,k}\Big) \\ &+ \frac{2}{\Delta t}\sum_{k=1}^{N_n}W_{mj}N_{mk}\Big(h_k(t)\Big)\Big]w_m\Delta_m\Big\} \end{aligned} \tag{3.11b}$$

$$\begin{aligned} C_j = &-\sum_{n=1}^{N_e}\Big\{\sum_{m=1}^{N_{gp}}\Big[W_{mj}\frac{\partial}{\partial x}\Big(f(p)_m h_m(U+u_{s,m})\Big) + W_{mj}\Big(\frac{\partial N_{mk}}{\partial y}r_k h_k v_{s,k}\Big)\Big] \\ &+ \Big[\frac{2}{\Delta t}W_{mj}\Big(f(p(t))_m h(t)_m - f(p(t-\Delta t))_m h(t-\Delta t)_m\Big) \\ &+ \frac{2}{\Delta t}W_{mj}\sum_{k=1}^{N_n}N_{mk}\Big(r_k(t-\Delta t)h_k(t-\Delta t)\Big)\Big]w_m\Delta_m\Big\} \end{aligned} \tag{3.11c}$$

One final step is necessary before solving the above system of linear algebraic equations. The pressure boundary conditions need to be processed into the A matrix. By inverting the matrix A and multiplying it with the equation (3.10) pressure can be expressed as,

$$p = -[A]^{-1}[B]r - [A]^{-1}[C] \tag{3.12}$$

or alternatively

$$p = [L]r + [Q] \tag{3.13}$$

Equation (3.13) is now ready to be solved by using a pivoting algorithm. The details of the numerical solver will be given in the following sections.

3.2 Numerical method for fixed N-direction boundary slippage problem

Finite element method, Galerkin method, is implemented to solve the equation (2.27) with complementary variables of (2.28). Slip velocity and shear stress equations are written for each slip direction, so there is N number of equations. These equations are coupled because shear stress in any direction depends on slip velocity in all directions. For ease of solution, first, we will discretize the generic equation, and then these equations will be combined and solved under a single matrix system. In equation (3.14), the upper index D is used to express the slip directions and takes integer values from 1 to N. Assuming a general test function W, equation (2.27) is first multiplied by it and then integrated over the entire domain.

$$\int_\Omega W\Bigg[\gamma^D - \frac{h}{2}\left(\frac{\partial p}{\partial x}cos(\beta^D) + \frac{\partial p}{\partial y}sin(\beta^D)\right) + U\frac{\mu}{h}cos(\beta^D) - \tau_c \\ - \frac{\mu}{h}\left(cos(\beta^D)(\sum_D^N \lambda^D \cdot cos\beta^D) + sin(\beta^D)(\sum_D^N \lambda^D \cdot sin\beta^D)\right)\Bigg] d\Omega = 0 \tag{3.14}$$

Separation of individual terms result in,

$$\int_\Omega W\gamma^D d\Omega - \int_\Omega W\frac{h}{2}\Big(\frac{\partial p}{\partial x}cos(\beta^D) + \frac{\partial p}{\partial y}sin(\beta^D)\Big)d\Omega - \int_\Omega W\tau_c d\Omega \\ - \int_\Omega W\left(cos(\beta^D)(\sum_D^N \lambda^D \cdot cos\beta^D) + sin(\beta^D)(\sum_D^N \lambda^D \cdot sin\beta^D)\right)d\Omega \\ + \int_\Omega WU\frac{\mu}{h}cos(\beta^D)d\Omega = 0 \tag{3.15}$$

Since the order of the differential equation is one, no further reduction operation is necessary. The two-dimensional solution domain is partitioned into a finite number of elements, and equation (3.15) is discretized over each element. The unknown variables γ^D and λ^D can be interpolated inside each element of the domain with shape functions.

$$\gamma^D = \sum_{i=1}^{N_n} N_i \gamma_i^D \tag{3.16a}$$

$$\lambda^D = \sum_{i=1}^{N_n} N_i \lambda_i^D \tag{3.16b}$$

where N_n is the number of nodes per element and N_i is the proper shape function. Bilinear shape functions can be used for interpolations; see equation (3.6). Standard Galerkin approximation is followed, and test functions that are the same as the shape functions are used. The integrals of equation (3.15) is evaluated numerically by Gaussian quadrature rule and discretized on the jth node of the element Ω_e.

$$\begin{aligned}
F_j(\Omega_e) = &+ \sum_{m=1}^{N_{gp}} \Big[\sum_{k=1}^{N_n} W_{mj} N_{mk} \gamma_k^D \Big] w_m \Delta\Omega_m \\
&- \sum_{m=1}^{N_{gp}} \Big[\sum_{k=1}^{N_n} \sum_{M=1}^{N} W_{mj} N_{mk} \Big(\lambda_M cos(\beta^D) cos(\beta^M) + \lambda_M sin(\beta^D) sin(\beta^M) \Big) \lambda_k^D \Big] w_m \Delta\Omega_m \\
&- \sum_{m=1}^{N_{gp}} W_{mj} \Big[\frac{h_m}{2} (\frac{\partial p}{\partial x})_m cos(\beta^D)_m + \frac{h_m}{2} (\frac{\partial p}{\partial y})_m sin(\beta^D)_m \Big] w_m \Delta\Omega_m \\
&+ \sum_{m=1}^{N_{gp}} W_{mj} \Big[U \frac{\mu_m}{h_m} cos(\beta^D)_m \Big] w_m \Delta\Omega_m \\
&- \sum_{m=1}^{N_{gp}} W_{mj} \Big[\tau_c \Big] w_m \Delta\Omega_m \\
&= 0
\end{aligned} \tag{3.17}$$

This equation has three different terms: the γ variable multipliers, λ variable multipliers, and the last one is free terms. When equation (3.17) is written for each point of the system, it takes the following form.

$$[X^D]\gamma^D + [Y^{D,1}]\lambda^{D,1} + [Y^{D,2}]\lambda^{D,2} + ... + [Y^{D,N}]\lambda^{D,N} + [Z^D] = 0 \tag{3.18}$$

where

$$X_{j,k}^D = \sum_{n=1}^{N_e} \Big\{ \sum_{m=1}^{N_{gp}} \Big[\sum_{k=1}^{N_n} W_{mj} N_{mk} \Big] w_m \Delta\Omega_m \Big\} \tag{3.19a}$$

$$Y_{j,k}^{D,M} = - \sum_{n=1}^{N_e} \Big\{ \sum_{m=1}^{N_{gp}} \Big[\sum_{k=1}^{N_n} W_{mj} N_{mk} \Big(cos(\beta^D) cos(\beta^M) + sin(\beta^D) sin(\beta^M) \Big) \Big] w_m \Delta\Omega_m \Big\} \tag{3.19b}$$

$$Z_j^D = -\sum_{n=1}^{N_e}\Big\{\sum_{m=1}^{N_{gp}} W_{mj}\Big[\frac{h_m}{2}(\frac{\partial p}{\partial x})_m cos(\beta^D)_m + \frac{h_m}{2}(\frac{\partial p}{\partial y})_m sin(\beta^D)_m + U\frac{\mu_m}{h_m}cos(\beta^D)_m + \tau_c\Big] w_m \Delta\Omega_m\Big\} \tag{3.19c}$$

If equation (3.18) is written for N number of directions and collected under a single, larger matrix system, it takes the following form,

$$\begin{bmatrix} X^1 & & & & & \\ & X^2 & & & & \\ & & X^3 & & & \\ & & & . & & \\ & & & & . & \\ & & & & & X^N \end{bmatrix} \begin{bmatrix} \gamma^1 \\ \gamma^2 \\ \gamma^3 \\ . \\ . \\ . \\ \gamma^N \end{bmatrix} + \begin{bmatrix} Y^{1,1} & Y^{1,2} & Y^{1,3} & . & . & . \\ Y^{2,1} & Y^{2,2} & Y^{2,3} & & & . \\ Y^{3,1} & Y^{3,2} & Y^{3,3} & & & . \\ . & & & & . & . \\ . & & & & & . \\ . & . & . & . & . & Y^{D,M} \end{bmatrix} \begin{bmatrix} \lambda^1 \\ \lambda^2 \\ \lambda^3 \\ . \\ . \\ \lambda^N \end{bmatrix} + \begin{bmatrix} Z^1 \\ Z^2 \\ Z^3 \\ . \\ . \\ Z^N \end{bmatrix} = 0 \tag{3.20}$$

where each element here is a smaller matrices. Alternatively it can be expressed as,

$$[E]\gamma + [F]\lambda + [H] = 0 \tag{3.21}$$

Since there are no boundary conditions for the slip problem, no modifications are necessary to solve the above system of linear algebraic equations. By inverting the matrix E and multiplying it with the equation (3.21) γ can be expressed as,

$$\gamma = -[E]^{-1}[F]\lambda - [E]^{-1}[H] \tag{3.22}$$

or alternatively,

$$\gamma = [L_s]\lambda + [Q_s] \tag{3.23}$$

Equation (3.23) is now ready to be solved, by using pivoting algorithm.

3.3 Numerical method for rotating 3-direction boundary slippage problem

Finite element method, Galerkin method, is implemented to solve the equation (2.31) with complementary conditions of (2.32). The slip velocity and shear stress

equations are written for each slip direction, so there are three equations. These equations are not coupled; however, for ease of solution, first, we will discretize the generic equation, and then these equations will be combined and solved under a single matrix system. In equation (3.24), the upper index D is used to express the slip directions and takes integer values from 1 to 3. Assuming a general test function W, equation (2.27) is first multiplied by it and then integrated over the entire domain.

$$\int_{\Omega} W\Big[\gamma^D - \frac{h}{2}(\frac{\partial p}{\partial x}cos(\beta^D) + \frac{\partial p}{\partial y}sin(\beta^D)) - \frac{\mu}{h}\lambda^D - U\frac{\mu}{h}cos(\beta^D) - \tau_c\Big]d\Omega = 0 \tag{3.24}$$

Separation of individual terms result in,

$$\begin{aligned}\int_{\Omega} W\gamma^D d\Omega - \int_{\Omega} W\frac{h}{2}\Big(\frac{\partial p}{\partial x}cos(\beta^D) + \frac{\partial p}{\partial y}sin(\beta^D)\Big)d\Omega \\ - \int_{\Omega} W\frac{\mu}{h}\lambda^D d\Omega - \int_{\Omega} WU\frac{\mu}{h}cos(\beta^D)d\Omega - \int_{\Omega} W\tau_c d\Omega = 0\end{aligned} \tag{3.25}$$

Since the order of the differential equation is one, no further reduction operation is necessary. The two-dimensional solution domain is partitioned into a finite number of elements, and equation (3.25) is discretized over each element. The unknown variables of (3.25), γ^D and λ^D can be interpolated inside each element of the domain with shape functions.

$$\gamma^D = \sum_{i=1}^{N_n} N_i \gamma_i^D \tag{3.26a}$$

$$\lambda^D = \sum_{i=1}^{N_n} N_i \lambda_i^D \tag{3.26b}$$

where N_n is the number of nodes per element and N_i is the proper shape function. Bilinear shape functions can be used for interpolations; see equation (3.6). Standard Galerkin approximation is followed, and test functions that are the same as the shape functions are used. The integrals of equation (3.25) are evaluated numerically by Gaussian quadrature rule and discretized on the jth node of the

element Ω_e.

$$\begin{aligned} F_j(\Omega_e) = &+ \sum_{m=1}^{N_{gp}} \Big[\sum_{k=1}^{N_n} W_{mj} N_{mk} \gamma_k^D \Big] w_m \Delta\Omega_m \\ &- \sum_{m=1}^{N_{gp}} \Big[\sum_{k=1}^{N_n} W_{mj} N_{mk} \lambda_k^D \Big] w_m \Delta\Omega_m \\ &- \sum_{m=1}^{N_{gp}} W_{mj} \Big[\frac{h_m}{2} (\frac{\partial p}{\partial x})_m cos(\beta^D)_m + \frac{h_m}{2} (\frac{\partial p}{\partial y})_m sin(\beta^D)_m \Big] w_m \Delta\Omega_m \\ &- \sum_{m=1}^{N_{gp}} W_{mj} \Big[U \frac{\mu_m}{h_m} cos(\beta^D)_m \Big] w_m \Delta\Omega_m \\ &- \sum_{m=1}^{N_{gp}} W_{mj} \Big[\tau_c \Big] w_m \Delta\Omega_m \\ &= 0 \end{aligned} \tag{3.27}$$

This equation has three different terms: the γ variable multipliers, the λ variable multipliers, and the last one is free terms. When equation (3.27) is written for each point of the system, it takes the following form.

$$[X^D]\gamma^D + [Y^D]\lambda^D + [Z^D] = 0 \tag{3.28}$$

where

$$X_{j,k}^D = \sum_{n=1}^{N_e} \Big\{ \sum_{m=1}^{N_{gp}} \Big[\sum_{k=1}^{N_n} W_{mj} N_{mk} \gamma_k^D \Big] w_m \Delta\Omega_m \Big\} \tag{3.29a}$$

$$Y_{j,k}^D = - \sum_{n=1}^{N_e} \Big\{ \sum_{m=1}^{N_{gp}} \Big[\sum_{k=1}^{N_n} W_{mj} N_{mk} \lambda_k^D \Big] w_m \Delta\Omega_m \Big\} \tag{3.29b}$$

$$\begin{aligned} Z_j^D = - \sum_{n=1}^{N_e} \Big\{ \sum_{m=1}^{N_{gp}} W_{mj} \Big[&\frac{h_m}{2} (\frac{\partial p}{\partial x})_m cos(\beta^D)_m + \frac{h_m}{2} (\frac{\partial p}{\partial y})_m sin(\beta^D)_m \\ &+ U \frac{\mu_m}{h_m} cos(\beta^D)_m + \tau_c \Big] w_m \Delta\Omega_m \Big\} \end{aligned} \tag{3.29c}$$

If equation (3.28) is written for 3 different directions and collected under a single, larger matrix system, it takes the following form,

$$\begin{bmatrix} X^1 & & \\ & X^2 & \\ & & X^3 \end{bmatrix} \begin{bmatrix} \gamma^1 \\ \gamma^2 \\ \gamma^3 \end{bmatrix} + \begin{bmatrix} Y^1 & & \\ & Y^2 & \\ & & Y^3 \end{bmatrix} \begin{bmatrix} \lambda^1 \\ \lambda^2 \\ \lambda^3 \end{bmatrix} + \begin{bmatrix} Z^1 \\ Z^2 \\ Z^3 \end{bmatrix} = 0 \tag{3.30}$$

where each element here is a smaller matrices. Alternatively it can be expressed as,

$$[E]\gamma + [F]\lambda + [H] = 0 \tag{3.31}$$

Since there are no boundary conditions for the slip problem, no modifications are necessary to solve the above system of linear algebraic equations. By inverting the matrix E and multiplying it with the equation (3.31) γ can be expressed as,

$$\gamma = -[E]^{-1}[F]\lambda - [E]^{-1}[H] \tag{3.32}$$

or alternatively,

$$\gamma = [L_s]\lambda + [Q_s] \tag{3.33}$$

Equation (3.33) is now ready to be solved, by using pivoting algorithm.

3.4 Algorithm description

In this section, the details of the explicit algorithm will be given. The algorithm is available in four main loops, although not every problem requires all of them. In the first cycle cavitation problem is calculated; in the second cycle, the slip velocities are calculated; in the third cycle, slip directions are updated; and in the last one system marches in time. At the beginning of the problem, it should be noted that the direction and speed of the slip are not known prior. However, the solution to the cavitation problem depends on these values. Some unknown values will be assumed, and to give explicitly the solution.

3.4.1 Fixed N-direction slip algorithm

For the fixed N-direction slip model, three primary solution loops are present. See figure, 3.1, 3.2 for the flow charts of steady state and transient algorithms respectively.

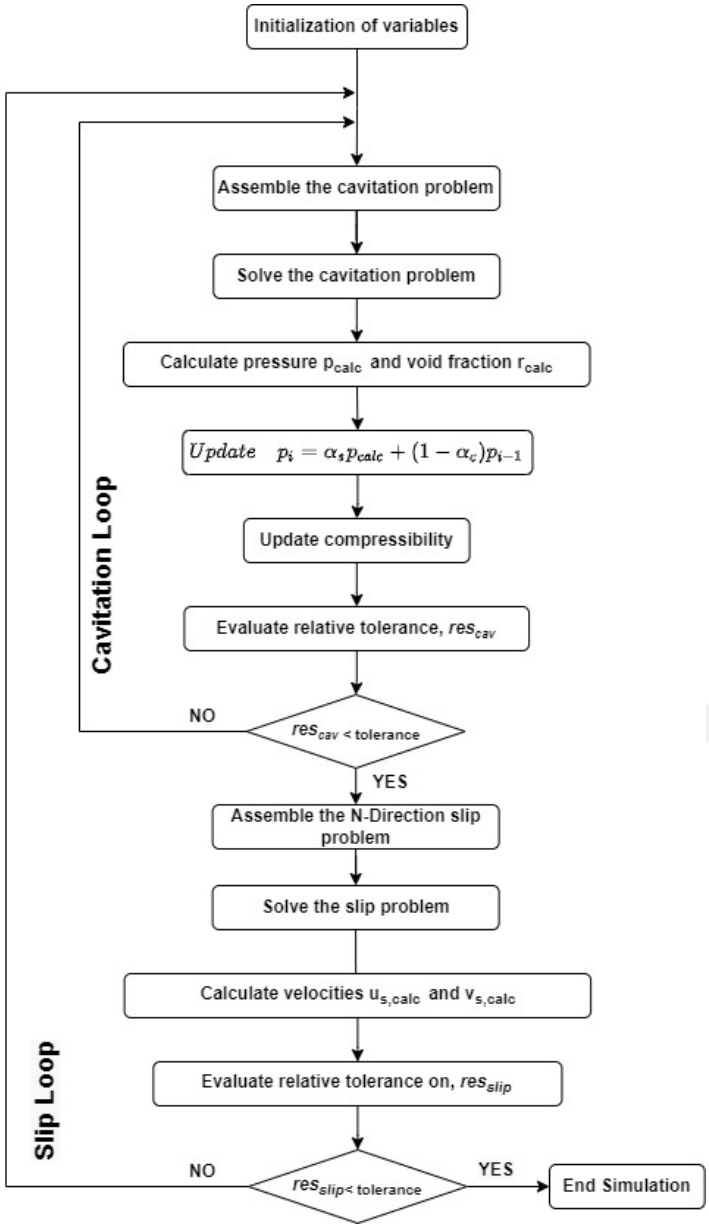

Figure 3.1: The flow chart of the steady state fixed N-direction slip algorithm.

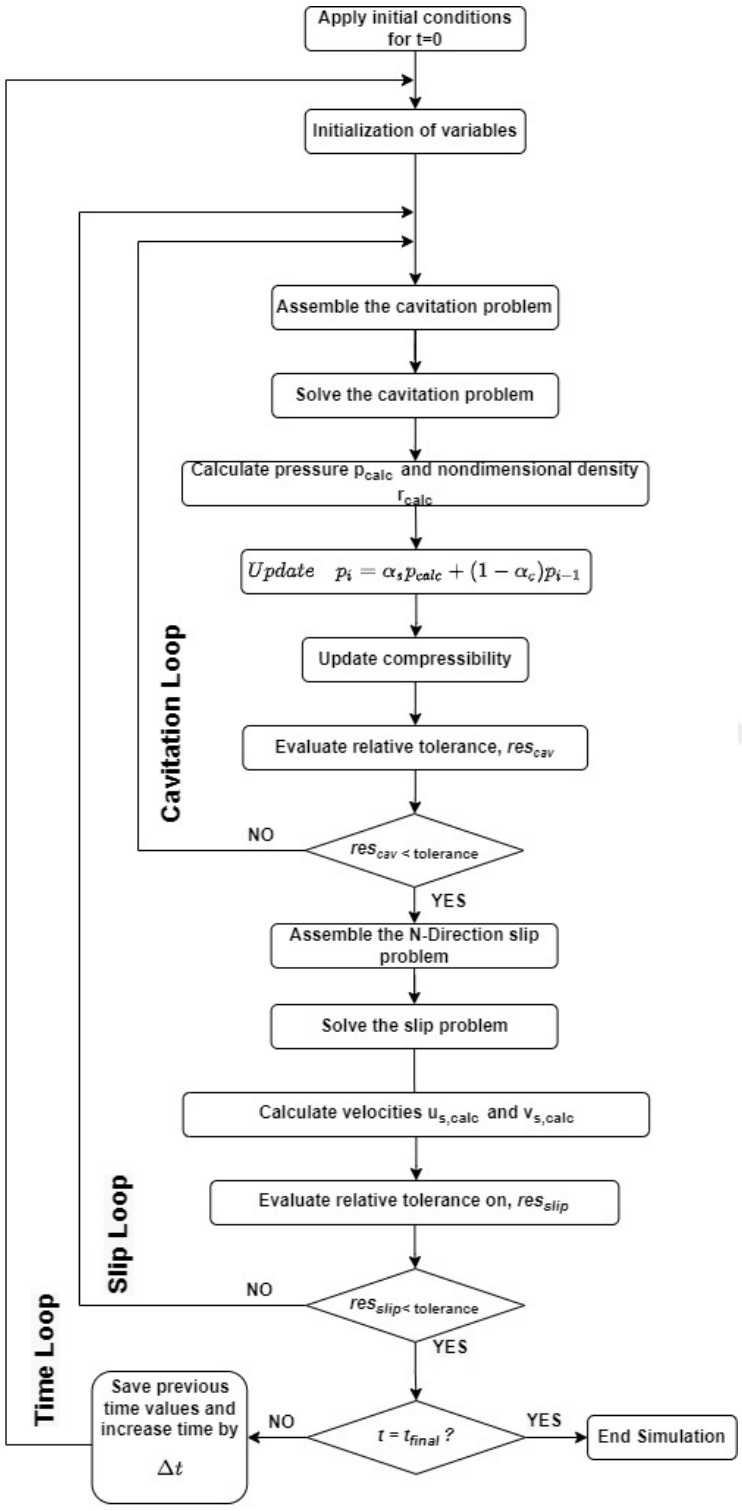

Figure 3.2: The flow chart of the transient fixed N-direction slip algorithm.

3.4.1.1 Cavitation loop

The cavitation problem has four unknowns. These are pressure, density and compressibility respectively. Compressibility depends on pressure; therefore, all can be calculated by finding the correct pressure values. Pressure and density values are calculated with initial compressibility assumption. Then, compressibility is updated with newly found pressure values. This cycle continues until the pressure values converge to a solution. At this point, the correct pressure and void ratio for the slip velocity and directions assumptions are found.

3.4.1.2 Slip Velocity loop

The slip velocity problem has a 2N number of unknowns, slip velocities, and shear stresses in each direction. First, the cavitation cycle will take place, and the pressure values will be found, then the slip velocities will be calculated with these pressure values. Later these calculated slip velocities will be used to correct the pressure values in the next cavitation cycle. This cycle will continue until the correct pressure and slip velocities are found. Due to the explicit nature of the problem, the pressure values are under-relaxed while updating in order for the problem to converge. It has been found that 0.4 is the optimal under-relaxation factor. If no under relaxation is used, the solution diverges. For the fixed N-direction slip model, the correct pressure, void ratio, and slip velocities are found.

3.4.1.3 Transient loop

Finally, there is the time loop for transient problems. The transient algorithm solves the problem with certain time intervals. For each time interval, all of the loops mentioned above work. The program is finished when the last time is reached.

3.4.2 Rotating 3-direction slip algorithm

For the rotating 3-direction slip model, four primary solution loops are present. See figure, 3.3 and 3.4 for the flow charts of steady state and transient algorithms respectively. All the loops described in the fixed N-direction slip model works for rotating the 3-direction slip model. One additional loop is required to update the direction of the slippage.

3.4.2.1 Slip Direction loop (rotation loop)

This cycle exists only for the rotating 3-Direction slip model. The slip direction will be calculated by rotating the system in this cycle. In the calculations, only the values in the first slip direction will be used, and the second and third slip directions will be used to understand in which direction the system should be rotated. If the surface shear stress in the second direction is greater than the third, the system will be rotated counterclockwise. However, if the shear stress in the third direction is greater than the second, the system will be rotated clockwise. The shift in each loop will be made by a fixed angle, β_r. If all the nodes do not rotate further in any direction, the correct slip angle is found. See figure 3.3 and 3.4.

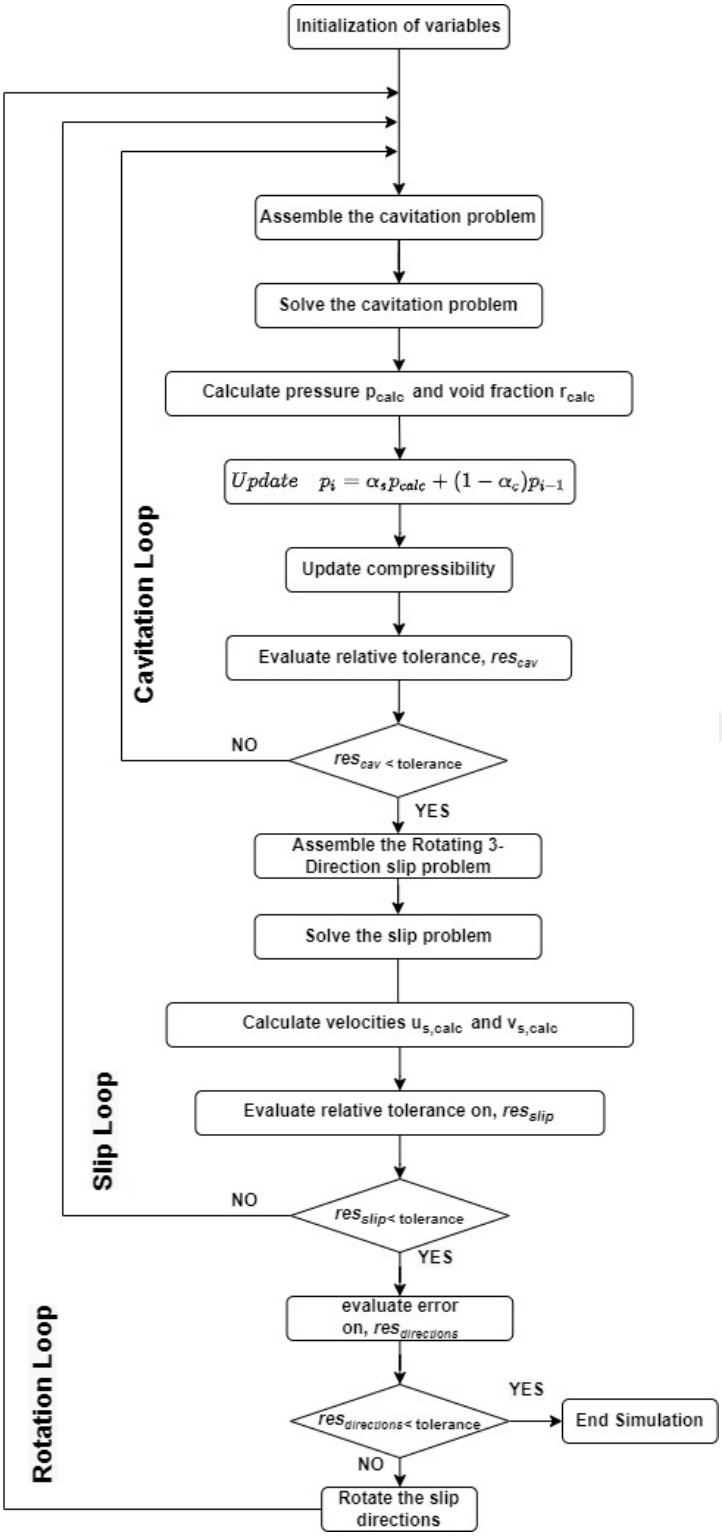

Figure 3.3: The flow chart of the steady state rotating 3-direction slip algorithm.

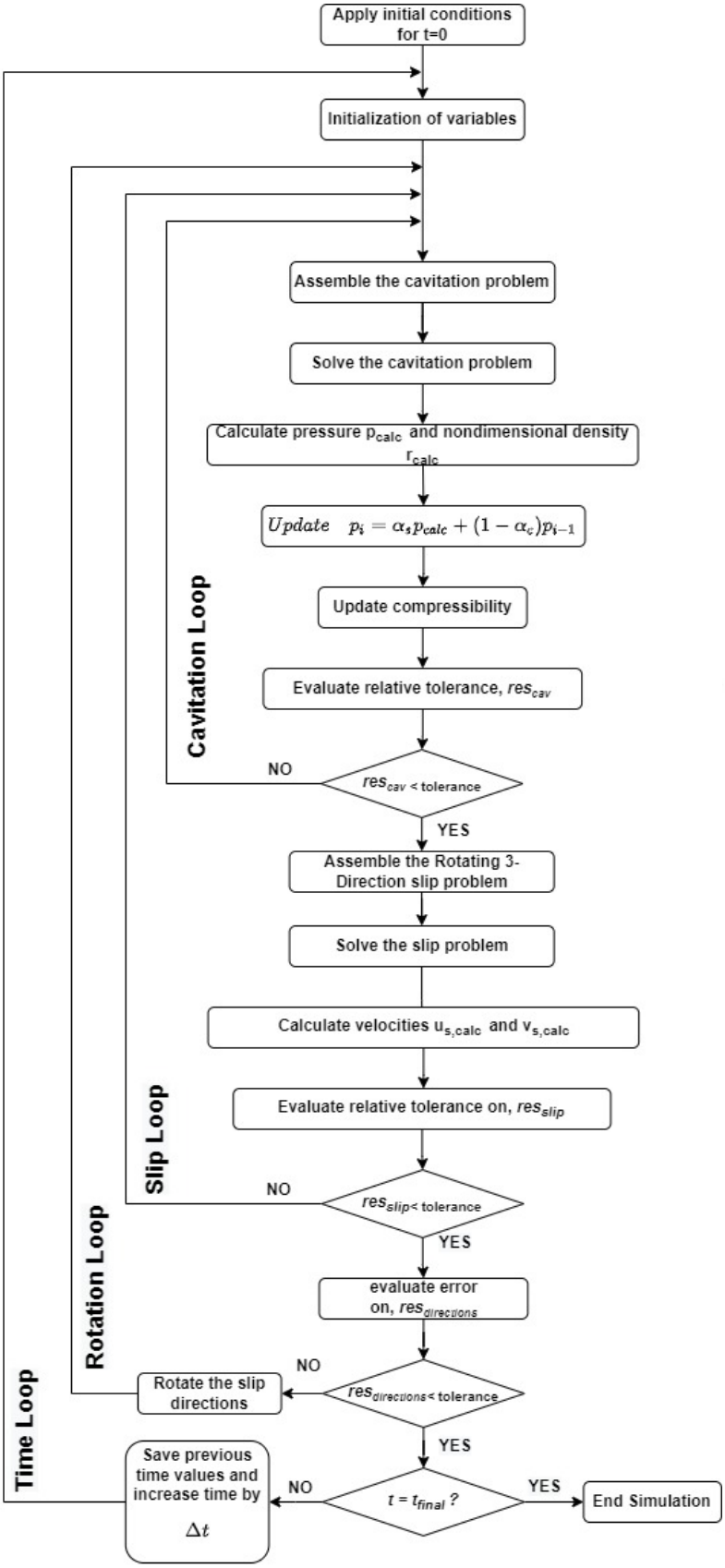

Figure 3.4: The flow chart of the transient rotating 3-Direction slip algorithm.

3.5 Numerical solver

Equations (3.13), (3.23) and (3.33) can be solved by proper pivoting algorithm. This study follows the pivoting algorithm proposed by Giacopini et al.. A brief explanation will be provided here. For details see, [41]. Assume a generic system of linear equations with complementary variables of Φ and Ω in the following form:

$$\Phi = [L]\Omega + [Q] \tag{3.34}$$

In the above system initially, Φ is defined as a basic variable, and Ω is the non-basic variable. Expanding matrix system for the i'th equation:

$$\Phi_i = [L]_{i,m}\Omega_m + [Q]_m, \quad m = 1, 2, ..., N^n \tag{3.35}$$

The pivoting algorithm works in the following order,

1. In equation (3.34), i'th equation is solved for i'th basic variable by assuming all the non-basic variables equal to zero. If the basic variables obey the linear complementary condition, i.e., greater than zero, the solution is found, and the algorithm is terminated. If not, proceed with the second stage.

2. If some of the basic variables do not obey the linear complementary condition, i.e., they are less than zero, pivoting operation is carried out with most unacceptable basic variable, See [53]. Let us assume j'th equation is to be pivoted; then, j'th non-basic variable of the other equations are replaced by j'th equation. This procedure converts the previous j'th non-basic variable to the basic variable and j'th basic variable to the non-basic variable. Then stage 1 is repeated.

One situation needs to be addressed. Pivoting ensures that the j'th equation matches the complementary condition; however, converting variables may force another equation that was satisfying the complementary condition previously to dissatisfy. Prepivoting is performed on the rest of the variables to prevent such cases. A detailed example for two equations and two node system is provided in [41].

Chapter 4

Numerical results

First, the mass-conserving linear complementary cavitation model and the multi-linearity slip models will be tested with the results available in the literature to validate whether they work accurately together with an explicit solution algorithm. Slider bearings in which other effects are not present and journal bearings in which cavitation will occur due to converging-diverging geometric profile will be used. The same examples will be used to validate the new slip model presented in this paper, the rotating 3-direction slip model. The two slip models are expected to give the same answers in the perfect slip condition. After these verifications are provided, a bearing with a micro-texture pocket will be used to test the solution algorithm under more challenging conditions. The presence of pockets increases the load support of the bearing; however, it introduces a discontinued geometric profile that is difficult to solve. This example case is chosen to push the limits of our model. Finally, a transient example of a pure squeezing motion will be given. After confirming that our models work accurately, the computational time requirements of the fixed N-direction and the rotating 3-direction multi-linearity slip algorithms will be compared.

4.1 Slider bearing

This section will discuss the design parameters of a slider bearing, and a numerical example will be provided.

4.1.1 Design Parameters

In slider bearing, it is assumed that the lubricant separates the moving lower surface and the stationary upper surface. The lower surface is sliding with constant velocity U, see figure 2.1. Wall slip is limited to some regions of the upper surface. The lower surface and some parts of the upper surface have very high limiting shear stress that slip cannot occur. The rest of the surfaces are assumed to be coated with a super-hydrophobic material with zero critical shear stress. Due to the geometric structure of the slider bearings, cavitation is not possible within the film. Some of the two-dimensional example cases presented in [26] will be replicated to validate our model. The convergence ratio of the slider bearing in terms of its entrance and exit heights, h_1 and h_0 defined as,

$$\zeta = \frac{h_1}{h_0} - 1 \tag{4.1}$$

The equation of the gap height of the slide bearing is,

$$h(x) = \frac{h_1 - h_0}{L} \cdot x + h_1 \tag{4.2}$$

The non-dimensional friction drag on the x-direction is,

$$\hat{f} = \frac{h_0}{UBL\mu} f \tag{4.3}$$

where B and L are the width and length of the bearing. The non-dimensional load is,

$$\hat{W} = \frac{h_0}{UL\mu} W \tag{4.4}$$

Four different cases are examined. In case one, the no-slip condition is assumed on the upper surface. In case two, perfect slip is assumed everywhere on the upper surface. For the third and fourth cases, please see figure 4.1. The lubricant is assumed to be incompressible.

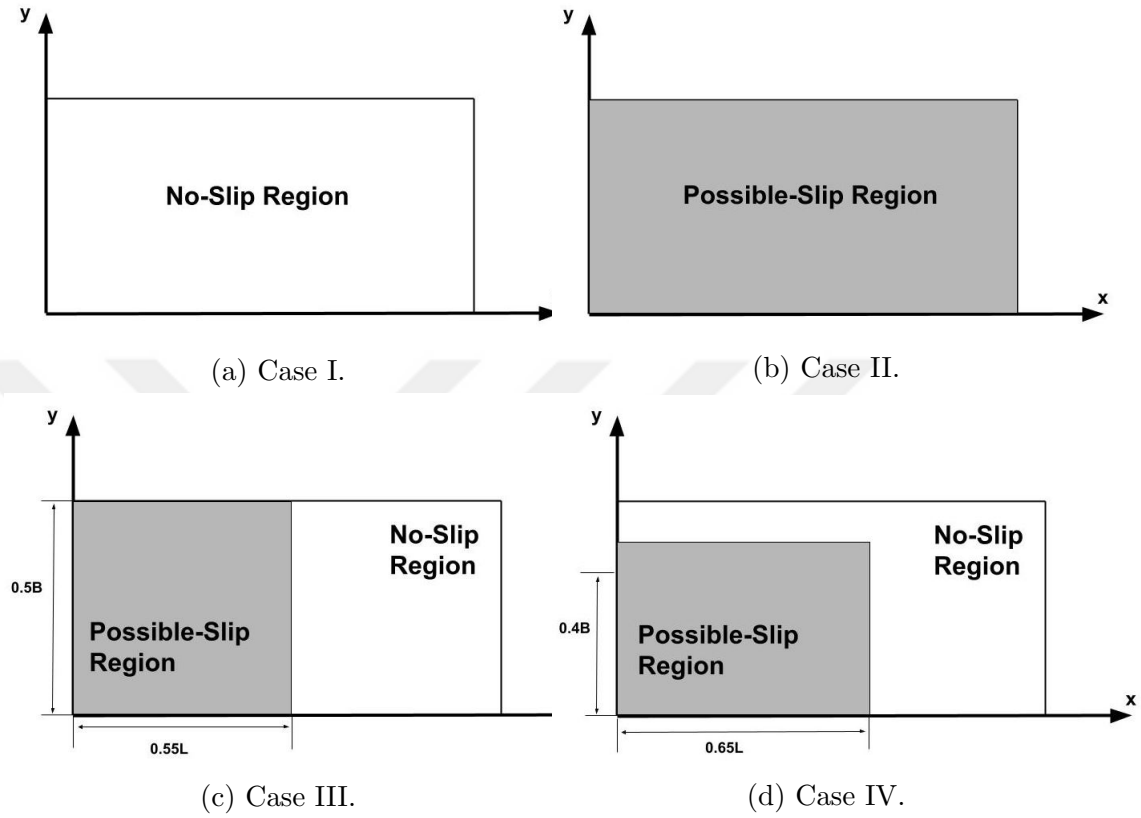

(a) Case I. (b) Case II.

(c) Case III. (d) Case IV.

Figure 4.1: Partial slip regions of the upper surface of the slider bearing, (a) case I, (b) case II, (c) case III, (d) case IV.

4.1.2 Numerical examples

To validate our model, slider bearing results of [26] will be replicated. G.J. Ma et al. use a multi-linearity slip algorithm to simulate boundary slippage. It should be noted that the fixed N-direction slip model is the one proposed by G.J. Ma. et al. An alternative multi-linearity model in which slip is limited to 3 directions that rotate to find the correct slip angle is proposed. First, results of [26] will be compared with the fixed N-direction slip model to validate our explicit algorithm, which involves a mass conserving cavitation model. Furthermore, the rotating 3-direction slip model proposed in this study will be tested to validate its accuracy. Parameters used for the simulation are presented at table 4.1. For cases, I and II, $\zeta = 1.3$ is used. For cases III and IV, $\zeta = 1$ is used. Half of the domain is computed since the problem is symmetric. eight hundred sixteen rectangular

elements are used to discretize the domain.

U	μ	p_a	p_c	h_1	B	L	τ_c	N_n
2	0.04	0	0	0.04	50	100	0	875
(m/s)	$(Pa \cdot s)$	(Pa)	(Pa)	(mm)	(mm)	(mm)	(Pa)	(-)

Table 4.1: Simulation parameters for slider bearing.

The pressure, slip direction and slip velocity magnitude profiles for case 2 as an example are given in figure 4.2.

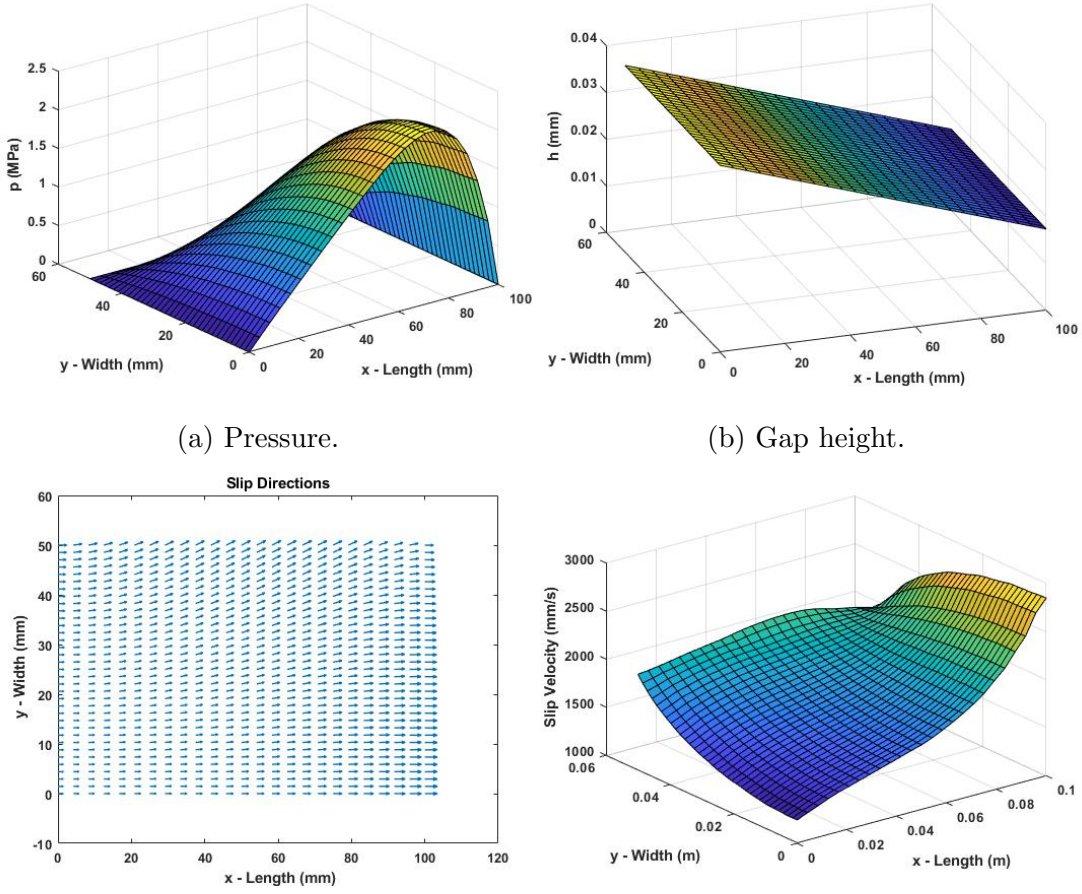

(a) Pressure.

(b) Gap height.

(c) Slip direction.

(d) Slip velocity.

Figure 4.2: Results of the slider bearing, case II, rotating 3-direction slip model, (a) pressure, (b) gap height, (c) slip direction, (d) slip velocity, $U = 2m/s$, $\mu = 0.04Pa \cdot s$, $\tau_c = 0Pa$, $L = 100mm$,$B = 50mm$,$P_a = P_c = 0$,$h_1 = 0.04mm$,$\zeta = 1.3$.

The non-dimensional load and friction values are reported in table 4.2 and 4.3 respectively.

Case Number	Results of [26]	Fixed N-direction model	Rotating 3-direction model
I	0.0698	0.0705	0.0705
II	0.0349	0.0358	0.0358
III	0.1218	0.1250	0.1254
IV	0.1588	0.1600	0.1612

Table 4.2: Comparison of non-dimensional load of the slider bearing for cases I,II,III and IV, $U = 2m/s$, $\mu = 0.04Pa \cdot s$, $\tau_c = 0Pa$, $L = 100mm$,$B = 50mm$,$P_a = P_c = 0$,$h_1 = 0.04mm$.

Case Number	Results of [26]	Fixed N-direction model	Rotating 3-direction model
I	0.6634	0.6866	0.6866
II	0.0340	0.0465	0.0464
III	0.5998	0.5858	0.5865
IV	0.6470	0.6539	0.6545

Table 4.3: Comparison of non-dimensional friction drag of the slider bearing for cases I,II,III and IV, $U = 2m/s$, $\mu = 0.04Pa \cdot s$, $\tau_c = 0Pa$, $L = 100mm$,$B = 50mm$,$P_a = P_c = 0$,$h_1 = 0.04mm$.

As it can be seen from table 4.2 and 4.3 results of fixed N-direction slip model are in a good agreement with [26]. Since there is no cavitation and the same slip models are used, the slight differences can be justified using different numerical methods. The results of the rotating 3-direction indicate that the model is predicting load and friction accurately (with an error of less than one percent). Covering the surface with super-hydrophobic material in slider bearing reduced the load and the friction drag, which is undesired. We want to increase the load to ensure the surfaces are not in contact and reduce the friction to prevent energy losses. Therefore, optimization is required to find the optimum setup. Even in cases with zero ζ (i.e., parallel gap), it has been observed that bearing creates a load with the effect of boundary slippage where traditional bearing cant produce hydrodynamic load support.

4.2 Journal bearings

This section will discuss the design parameters of a journal bearing, and numerical examples will be provided.

4.2.1 Design parameters

Analysis of journal bearings will begin by defining the design parameters. A lubricant separates the rotating rotor (journal) and stator (bearing) in journal bearings. If the rotor rotates at a sufficient speed, the pressure increases, providing hydrodynamic load support that is great enough to separate the rotor and the stator. The load will move the center of the rotor and cause a difference between the centers, also known as eccentricity. This change will lead to a converging-diverging geometry in which cavitation is possible. In this study, the journal bearing, generally examined in the radial coordinate system, will be cut and unwrapped from the point where the maximum gap height is and moved to the Cartesian coordinate system, see figure 4.4.

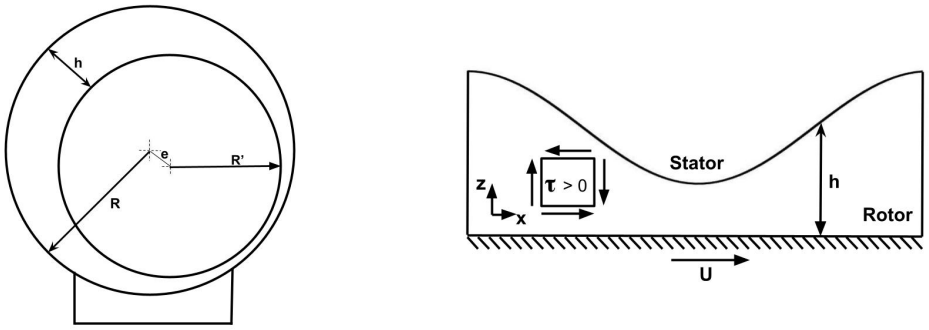

(a) Journal bearing in radial coordinate system.

(b) Journal bearing in Cartesian coordinate system.

Figure 4.3: Model for the journal bearing.

Only the rotor rotates with constant angular velocity ω therefore, the bottom

surface of the journal bearing in the cartesian coordinate system slides with constant velocity with $U = \omega \cdot R'$ where R' is the radius of the rotor. The negligible difference between the radius of the rotor and stator will be demonstrated as $c = R - R'$. Eccentricity ratio is defined as $\epsilon = \frac{e}{c}$. Using the design parameters given above, the equation of the geometry of the gap height in which the lubricant flows becomes as follows.

$$h(x) = c + e \cdot cos(\frac{x}{R'}) \tag{4.5}$$

For details of the derivation see, [3]. It has been assumed that the lower surface has a high limiting critical shear stress that boundary slippage cant take place. Some regions of the upper surface are assumed to be coated with superhydrophobic material that exhibits perfect slip (i.e., critical surface shear stress is zero). The details of the slip characteristics of the upper surface are given in figure 4.4.

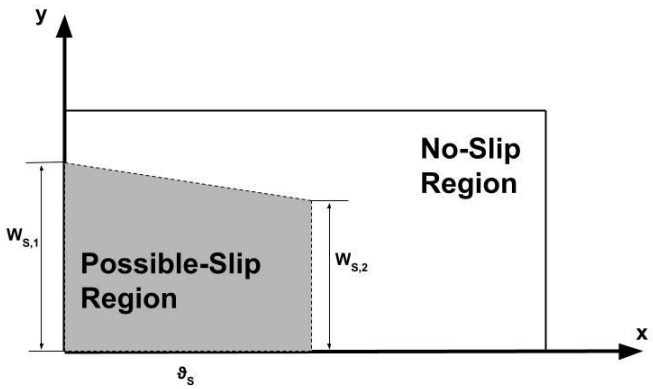

Figure 4.4: Partial slip region of the journal bearing.

Parameters Ω_s, $W_{s,1}$ and $W_{s,2}$ defines the slip region.

$$\Omega_s = \frac{x}{L} \cdot 2\pi \tag{4.6}$$

$$W_{s,i} = \frac{2y}{B} \tag{4.7}$$

The load support components in x and y directions are,

$$W_x = \int_0^B \int_0^L p \cdot sin(x) dx dy \tag{4.8}$$

$$W_y = \int_0^B \int_0^L p \cdot cos(x) dx dy \tag{4.9}$$

where L is the length of the bearing and B is the width of the bearing. The total load support is,

$$W = \sqrt{W_x^2 + W_y^2} \tag{4.10}$$

The friction drag on x axis at the bottom surface is,

$$f_x^{bottom} = \int_0^B \int_0^L \tau_x dx dy \tag{4.11}$$

Non dimensional parameters will be used to describe the characteristics of the journal bearing.

$$\hat{W} = -\frac{W c^2}{\mu \omega R^3 L} \tag{4.12}$$

$$\hat{f}_x^{Top} = \frac{f_x^{Top} c}{\mu \omega R^2 L} \tag{4.13}$$

$$\hat{f}_x^{bottom} = \frac{f_x^{Bottom} c}{\mu \omega R^2 L} \tag{4.14}$$

where $\hat{W}$, $\hat{f}_x^{Top}$ and $\hat{f}_x^{Bottom}$ are the non-dimensional load and friction drag on x direction, respectively. The lubricant is assumed to be incompressible.

4.2.2 Numerical examples

To validate our model, journal bearing results of [25] will be replicated. G.J. Ma et al. use a multi-linearity slip algorithm together with Reynolds condition to simulate cavitation. These results will be compared with the model proposed in this study. It should be noted that the fixed N-direction slip model (original multi-linearity model) used in this study is proposed by G.J. Ma. et al. Our cavitation model, which is mass conserving, will be tested with the N-direction slip model. Therefore even with the fixed N-direction slip model, a difference in the results is expected due to the cavitation model. Secondly, the alternative rotating 3-direction slip model proposed in this study will be tested. Parameters of the simulation are presented at table 4.4.

U	μ	p_a	p_c	c	L	B	N	τ_c	N_n
2	0.04	0	0	0.02	100	$100/\pi$	4	0	512
(m/s)	$(Pa \cdot s)$	(Pa)	(Pa)	(mm)	(mm)	(mm)	(-)	(Pa)	(-)

Table 4.4: Simulation parameters for journal bearings.

Simulations were made using the same parameters with nine different geometries (eccentricity values). For each eccentricity value, a different slip setup is used; see table 4.5.

ϵ	0	0.05	0.1	0.2	0.3	0.4	0.5	0.6	0.7	0.8
Ω_s	2.9	2.9	2.9	3	3	3.1	3.1	3.2	3.2	0.8
$W_{s,1}$	1	1	1	1	1	0.9	0.9	0.8	0.7	0.6
$W_{s,2}$	0.5	0.4	0.4	0.5	0.5	0.6	0.6	0.7	0.8	0.8

Table 4.5: Slip region setup for journal bearings.

As it was stated in [24],$N = 4$ is a good approximation for perfect slippage cases. The solution domain is divided into 465 rectangular elements. Since the problem is symmetric to the x-axis, only the solution domain's upper half is computed.

The pressure, void fraction, slip direction, and slip velocity magnitude profiles for $e = 0.0$ and $e = 0.6$ with a rotating 3-direction slip model are given. When the eccentricity ratio is zero, the cosine term in the equation 4.5 drops out, the upper and the lower surfaces become parallel to each other. One does not normally expect hydrodynamic load support in a parallel gap; however, boundary slippage (partially) accelerates the fluid layer adjacent to the upper surface and causes a pressure increase in the film, see figure 4.5a. No cavitation is observed, as expected from a parallel gap; see 4.5b. When the eccentricity ratio is set to 0.6, the converging-diverging profile creates a cavitation region on the diverging part of the bearing, see figure 4.6b.

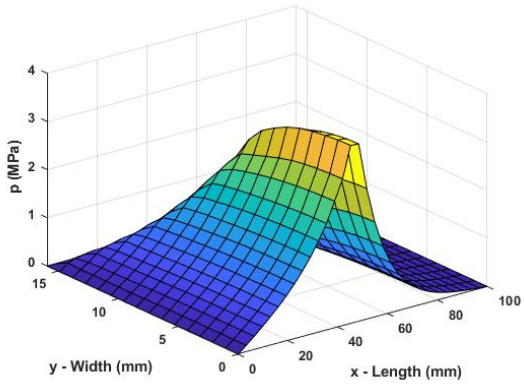

(a) Pressure.

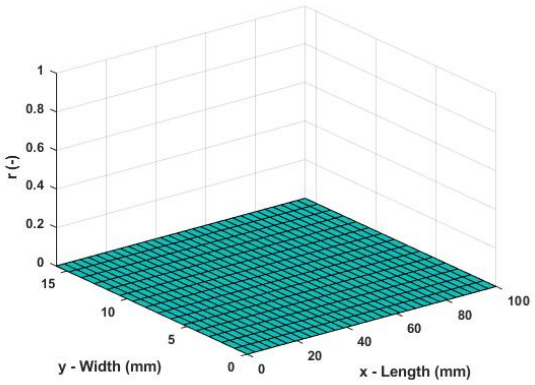

(b) Void fraction.

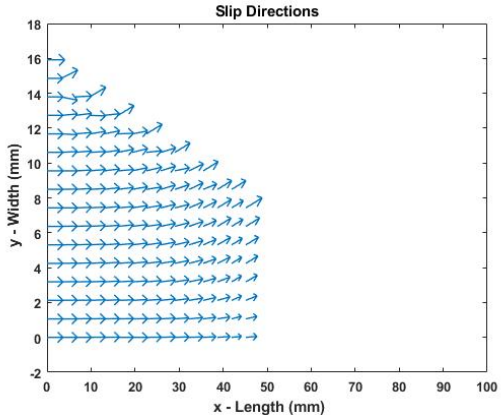

(c) Slip direction.

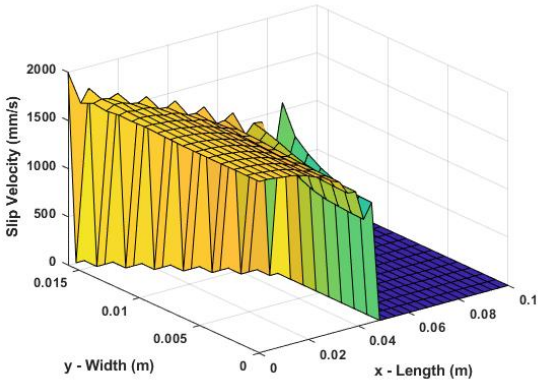

(d) Slip velocity.

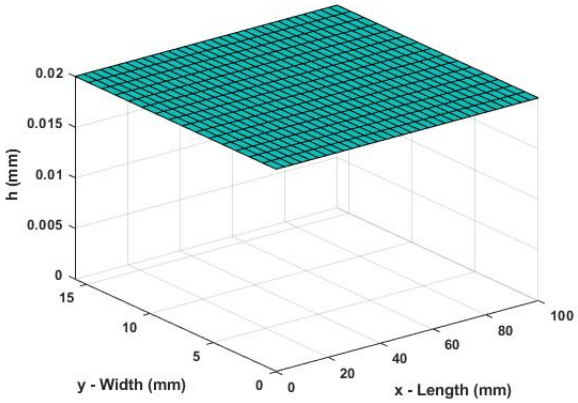

(e) Gap height.

Figure 4.5: Results of the journal bearing, $e = 0$, rotating 3-direction slip model, (a) pressure, (b) void fraction, (c) slip direction, (d) slip velocity, (e) gap height,$U = 2m/s$, $\mu = 0.04Pa \cdot s$, $\tau_c = 0Pa$, $L = 100mm$,$B = 100/\pi mm$,$P_a = P_c = 0$,$c = 0.02mm$,$N = 4$.

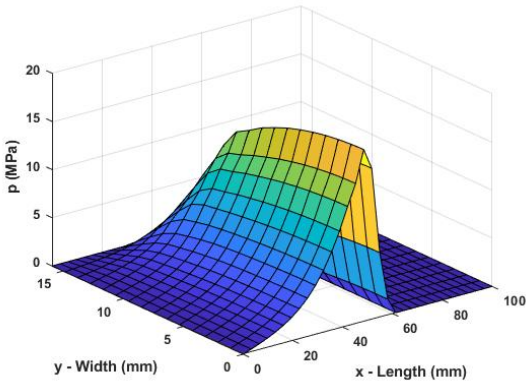

(a) Pressure.

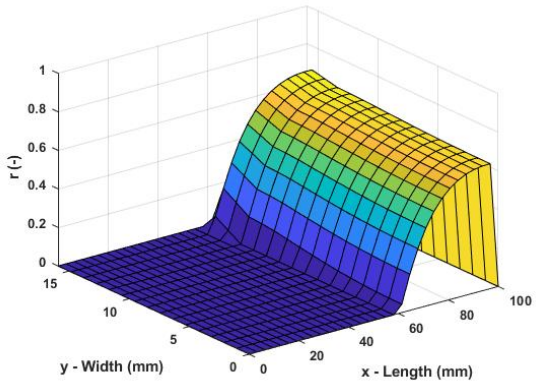

(b) Void fraction.

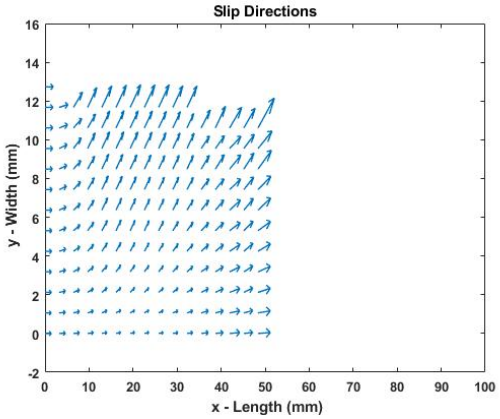

(c) Slip direction.

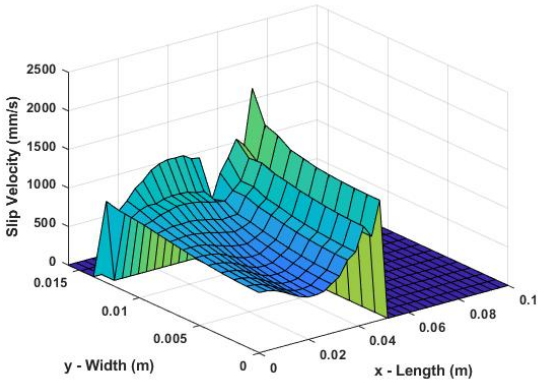

(d) Slip velocity.

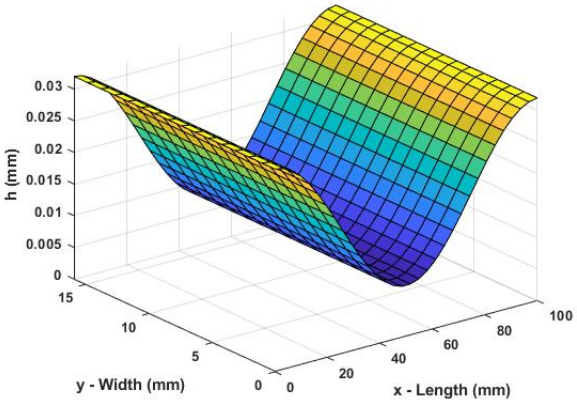

(e) Gap height.

Figure 4.6: Results of the journal bearing, $e = 0.6$, rotating 3-direction slip model, (a) pressure, (b) void fraction, (c) slip direction, (d) slip velocity, (e) gap height,$U = 2m/s$, $\mu = 0.04Pa \cdot s$, $\tau_c = 0Pa$, $L = 100mm$,$B = 100/\pi mm$,$P_a = P_c = 0$,$c = 0.02mm$,$N = 4$

Now the validation of our model will take place. First, we will look at the no-slip situations, analyze friction drag and hydrodynamic load. The load values of our model and [25] are reported in figure 4.7. Results are in good agreement with each other. There is an error of up to 5 % on higher eccentricity ratios which might be due to different cavitation models and numerical methods. In this study, a mass conserving linear complementary model is used, while in [25] Reynolds boundary condition is used. In figure 4.8, results of the slip problem, both the fixed N-direction slip model used in this study and the rotating 3-direction slip model proposed in this study are in good agreement with [25]. There exist an error of up to 5 % on higher eccentricity ratios between results of [25] and the fixed N-direction model. There is no notable difference between the fixed N-direction and rotating 3-direction slip models in terms of load. These results indicate that the slip model proposed in this study works accurately. Finally, the ratio of the loads in slip to no-slip cases is given in figure 4.9. In cases where the eccentricity ratio is low (or even on parallel surfaces where it is 0), great gains in load can be achieved thanks to the slip effect. This difference gradually disappears as eccentricity increases. After 0.9, the two cases give the same results. Similar results are obtained for friction drag. In a no-slip case, good agreement was achieved in friction drag values on x-direction at the lower surface, see figure 4.10. The differences, which are due to different cavitation models and numerical methods, are less than 5 %. In figure 4.11 friction values are reported for cases where slip is possible. The fixed N-direction slip model used in this paper gives similar results. There is no notable difference between the fixed N-direction slip model and the rotating 3-direction slip model in terms of friction. The slip model proposed in this study predicts friction values accurately. Finally, the ratio of the friction of slip to no-slip cases is given in figure 4.12. Boundary slippage reduced friction drag between 15 % and 30 %.

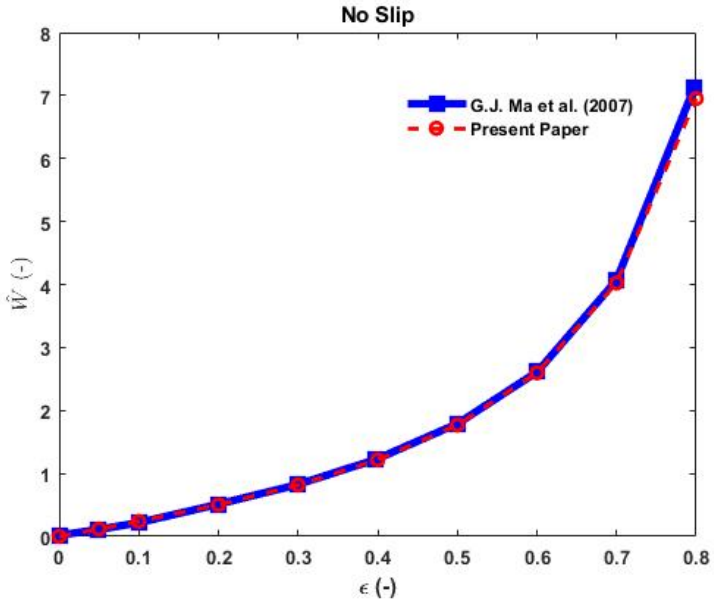

Figure 4.7: Non-dimensional load for different eccentricities, journal bearing, no slip case, $U = 2m/s$, $\mu = 0.04Pa \cdot s$, $\tau_c = 0Pa$, $L = 100mm$, $B = 100/\pi mm$, $P_a = P_c = 0$, $c = 0.02mm$, $N = 4$.

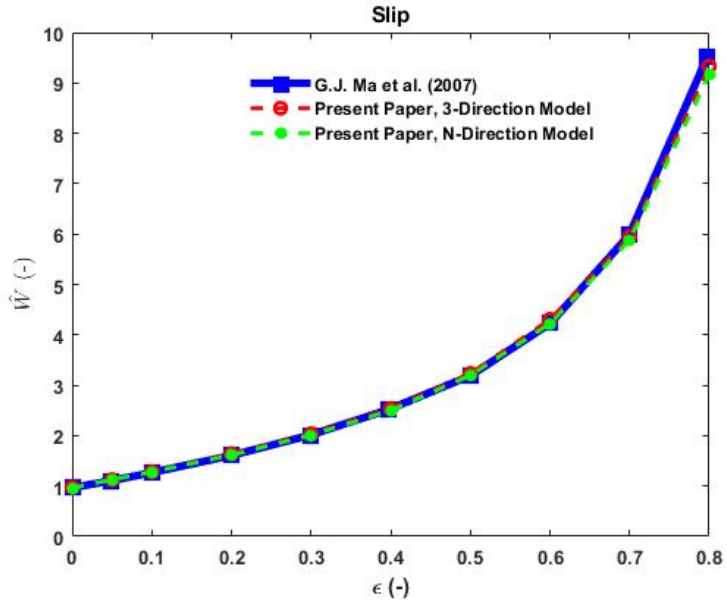

Figure 4.8: Non-dimensional load for different eccentricities, journal bearing, slip case, $U = 2m/s$, $\mu = 0.04Pa \cdot s$, $\tau_c = 0Pa$, $L = 100mm$, $B = 100/\pi mm$, $P_a = P_c = 0$, $c = 0.02mm$, $N = 4$.

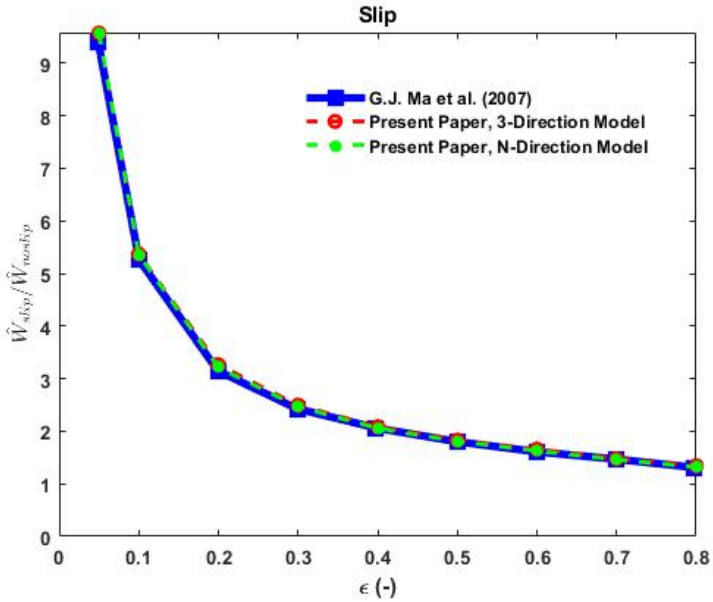

Figure 4.9: Ratios of non-dimensional load for different eccentricities, journal bearing, $U = 2m/s$, $\mu = 0.04Pa \cdot s$, $\tau_c = 0Pa$, $L = 100mm$, $B = 100/\pi mm$, $P_a = P_c = 0$, $c = 0.02mm$, $N = 4$.

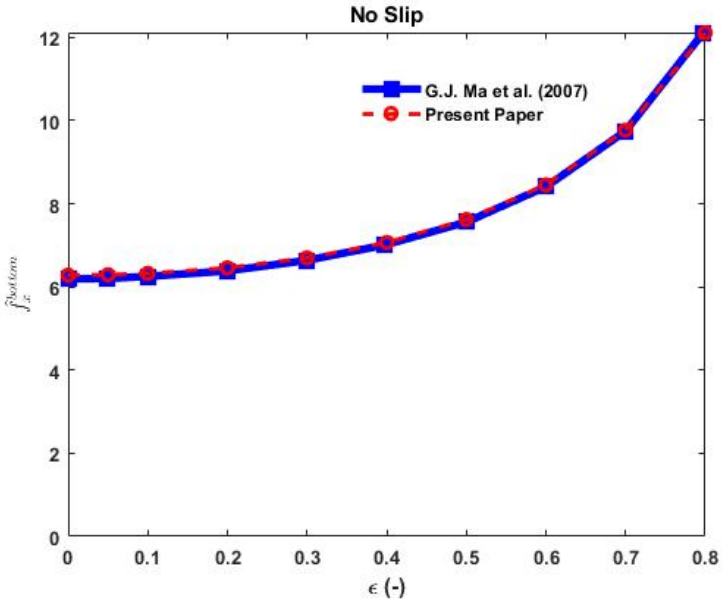

Figure 4.10: Non-dimensional friction drag for different eccentricities, journal bearing, no slip case, $U = 2m/s$, $\mu = 0.04Pa \cdot s$, $\tau_c = 0Pa$, $L = 100mm$, $B = 100/\pi mm$, $P_a = P_c = 0$, $c = 0.02mm$, $N = 4$.

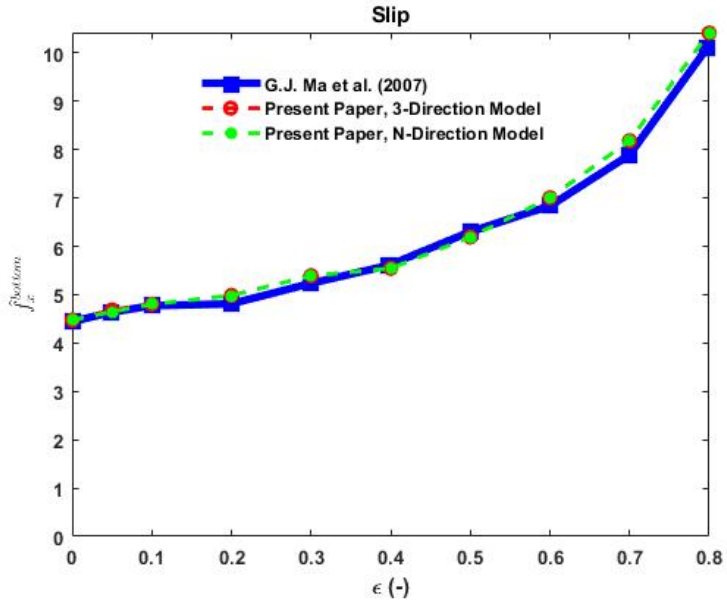

Figure 4.11: Non-dimensional friction drag for different eccentricities, journal bearing, slip case, $U = 2m/s$, $\mu = 0.04Pa \cdot s$, $\tau_c = 0Pa$, $L = 100mm$, $B = 100/\pi mm$, $P_a = P_c = 0$, $c = 0.02mm$, $N = 4$.

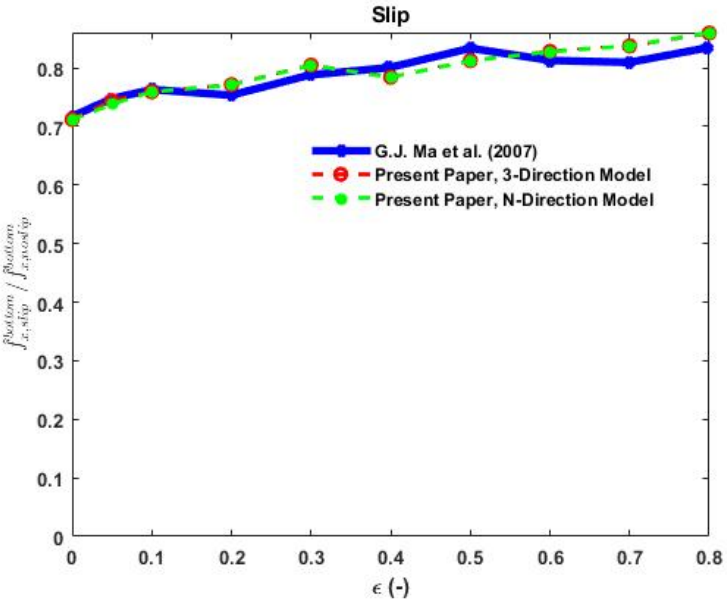

Figure 4.12: Ratios of non-dimensional friction drag for different eccentricities, journal bearing, $U = 2m/s$, $\mu = 0.04Pa \cdot s$, $\tau_c = 0Pa$, $L = 100mm$, $B = 100/\pi mm$, $P_a = P_c = 0$, $c = 0.02mm$, $N = 4$.

4.3 Slider bearing with micro texture pocket

This section will discuss the design parameters of a slider bearing with micro texture pocket, and a numerical example will be provided.

4.3.1 Design parameters

Microtexture pockets are placed on bearing surfaces to enhance the hydrodynamic load capacity of the bearings. The sharp change of the film height decreases the pressure to cavitation pressure on the pocket hole and causes the formation of cavities. Towards the end of the pocket, the pressure rises again and creates load support. The solution of the micro-texture pocket is relatively challenging because of the discontinuity of the geometric height of the film. Micro texture pockets are studied by L. Bertocchi et al.[42] and Ausas et al. [54]. A single pocket is placed on a slider bearing; see figure 4.13.

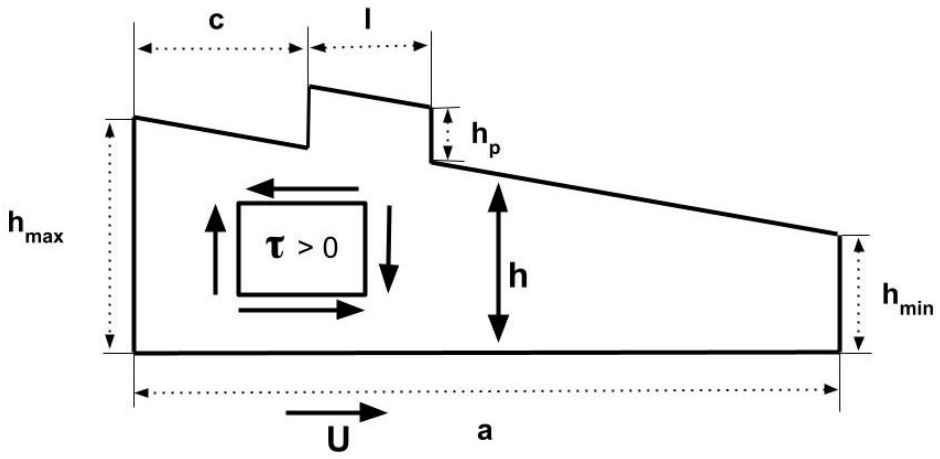

Figure 4.13: Model for the pocket slider.

The lower surface of the bearing is sliding with a constant velocity of 2 m/s. Perfect slip (i.e. $\tau_c = 0$) assumed on the last quarter of the upper surface. The lower surface of the bearing has high critical shear stress that slip cannot take place. The domain is discretized into 406 rectangular elements. Since the problem is symmetric, only one-half of the domain is computed. The load and friction drag

on the x-direction of the bearing are computed with the following formulations.

$$W = \int_0^B \int_0^L p \cdot dxdy \tag{4.15}$$

$$f = \int_0^B \int_0^L \tau_x \cdot dxdy \tag{4.16}$$

The load and friction are non-dimensionalized with respect to no slip cases. Downson and Higginson compressibility assumption is used.

4.3.2 Numerical example

The same pocket example from [42] is studied. The load and friction values are reported in table 4.6.

The parameters used are listed below,

- Length of the domain (L) : 20 mm
- Width of the domain (B) : 10 mm
- Length of the pocket (l) : 6 mm
- Width of the pocket (b) : 7 mm
- $h_{max} = 1.1$ μm
- $h_{max} = 1.1$ μm
- $h_p = 0.1$ μm
- c = 4 mm
- $p_a = 1$ bar
- $\mu = 0.01$ Pa $\cdot$ s

	W_{slip}/W_{noslip} (-)	f_{slip}/f_{noslip} (-)
N-Direction Slip Model	0.47	0.72
Rotating 3-Direction Slip Model	0.47	0.72

Table 4.6: Results of pocket bearing, $U = 2m/s$, $\mu = 0.01Pa \cdot s$, $\tau_c = 0Pa$, $P_a = P_c = 0$, $N = 4$.

Coating the downstream part of the bearing with super hydrophobic material reduced both load and friction. While there was a 53 percent decrease in load, there was a 28 percent decrease in friction drag. A more optimum surface setup for the pocket bearing can be found by optimization. The two slip models verify

each other by predicting the same load and friction values for the slider bearing with a single pocket.

4.4 Pure squeeze motion

This section will discuss the design parameters of pure squeeze motion of a thin film, and a numerical example will be provided.

4.4.1 Design parameters

Lastly, a transient example problem is solved. Initially, a lubricant stays between two parallel circular plates with a radius of r_a. Plates are first moved apart and then brought back to each other. During separation, pressure in film decreases to cavitation pressure for a short time, and cavities occur and grow in the center of the domain. Later, pressure increases, and cavitation collapses. The equation for the film height is,

$$h(t) = h_0 + h_a \cdot (1 - cos(\omega t)) \tag{4.17}$$

where h_0 is the initial height. A fully implicit time algorithm is used, and constant time steps of Δt are used to march in time. Non-dimensional cavitation radius ($\hat{x_c}$) and non-dimensional time ($\hat{t}$) is used to analyze the results.

$$\hat{x_c} = x_c / r_a \tag{4.18}$$

$$\hat{t} = \frac{t \cdot \omega}{2\pi} \tag{4.19}$$

Perfect slip (i.e. $\tau_c = 0$) assumed on the upper surface. The lower surface has high critical shear stress that slip cannot take place. Downson and Higginson compressibility assumption and constant viscosity assumption are used.

4.4.2 Numerical example

An example problem from [42] will be studied with boundary slippage. The radius of the plates is set to 5 mm. The viscosity of the lubricant is 0.005 Pa·s. h_0 and h_a are set to 320.8 μm and 9.14 μm respectively. The angular frequency of the periodic motion is 99.74 rad/s. Transient solution is divided into 384-time steps, and one complete periodic motion is studied. The cavitation radius over non-dimensional time is given in figure 4.14. It has been observed that boundary slippage causes the radius of cavitation to decrease and disappear earlier. During the separation of the two parallel circular discs, i.e., expansion of the film, the direction of the slip on the upper surface is from the outside of the circle to the center of the circle, and vice-a-versa during the squeezing of the film. The slipping took place symmetrically. In the numerical solutions, it was observed that the cavitation radius remained constant at certain time intervals. This situation arises due to the inadequacy of the mesh and time step used because the algorithm is limited by computational time.

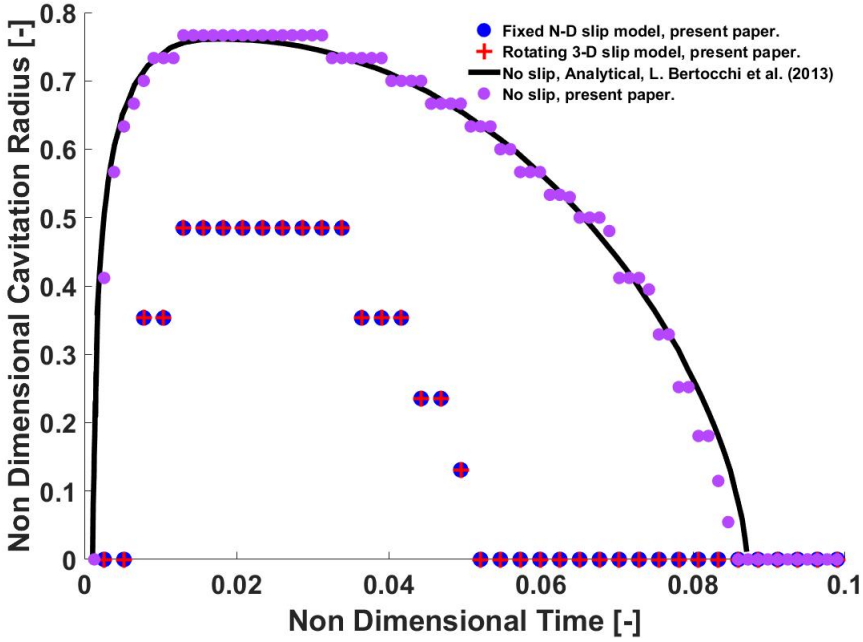

Figure 4.14: Non-dimensional cavitation radius over non-dimensional time.

4.5 Computational speed comparison of slip models

In this section, the computational time requirements of the fixed N-direction multi-linearity slip algorithm (proposed by [24]) and the rotating 3-direction multi-linearity slip algorithm will be compared. In the fixed N-direction model, the configuration that will give the same accuracy as the rotating 3-direction system will be found, and their computational times will be compared. The two models give the same result in the examples where the critical surface tension is 0, i.e., simulating the perfect slip condition. For this reason, a value other than zero will be chosen to reveal this difference. The journal bearing with an eccentricity value of 0.6 will be used; see figure 4.3. Other parameters to be used in the simulation are given below. The lubricant is assumed to be incompressible.

- Geometry: Journal bearing with eccentricity 0.6.
- Number of elements: 65 x 9 (660 nodes for the half of the domain, only one half is computed).
- Bearing Speed: 1 m/s
- Viscosity: 0.04 Pa·s
- Critical shear stress: 1 kPa
- L/D = 1
- L = 100mm
- p_a: 0 Pa
- Full slip region is used.

Non-dimensional load and friction and the error of fixed N direction slip model with respect to rotating 3 direction slip model is given below.

$$\%Error_W = \frac{W_{fixed,N-dir} - W_{rotating,3-dir}}{W_{rotating,3-dir}} \cdot 100 \tag{4.20}$$

$$\%Error_f = \frac{f_{fixed,N-dir} - f_{rotating,3-dir}}{f_{rotating,3-dir}} \cdot 100 \tag{4.21}$$

As shown from table 4.7, in order for the margin of error to fall below one percent, at least 16 directions must be used in the fixed N-direction slip model.

	W (-)	f (-)	$Error_W$	$Error_f$	Computational time
N=3	3.0631	3.4414	45.2 %	9.6 %	1.32 minutes
N=4	2.7554	3.3542	30.6 %	6.9 %	5.51 minutes
N=8	2.2213	3.2141	5.3 %	2.4 %	16.80 minutes
N=16	2.1148	3.1573	0.2 %	0.6 %	112.06 minutes
Rotating 3	2.1100	3.1387	-	-	12.20 minutes

Table 4.7: Comparison of accuracy and time trade-off of slip models, journal bearing eccentricity ratio 0.6, $U = 1m/s$, $\mu = 0.04Pa \cdot s$, $\tau_c = 1kPa$, $L = 100mm$, $B = 100/\pi mm$, $P_a = P_c = 0$, $c = 0.02mm$, $N = 3, 4, 8, 16, 32$.

The same answer can be obtained with the rotating 3-direction slip model. The calculation time of the rotating 3-direction model is 12.20 minutes, whereas, for the fixed N-direction model (N=16), it is 112.06 minutes. Therefore, in this example, the rotating 3-direction slip model proposed in this study is up to 9 times faster than the original slip model. It should be noted that the difference will be more significant if more elements are used. The rotating 3-direction model is more computationally affordable than the fixed N-direction slip model if the same accuracy is needed.

Chapter 5

Conclusions

Various algorithms have been proposed to understand the hydrodynamic characteristics of the thin lubricant film between two surfaces in relative motion. The basis point of these models starts with the Reynolds equation, which is a simplified version of the full Navier-Stokes equations. However, the Reynolds equation is not sufficient to simulate all the characteristic properties of the thin lubricant film, and modifications are required to reveal the effects of various other phenomena. In hydrodynamic lubrication, wall slip and hydrodynamic cavitation are the two phenomena, which can significantly change the lubricant pressure density and velocity values. An accurate mathematical model was created by combining these phenomena with the Reynolds equation in this thesis.

Miscellaneous models exist to simulate boundary slippage and cavitation phenomena into Reynolds Equation. As the literature review reveals, for the cavitation, the mass-conserving linear complementary cavitation model is chosen for its accuracy in predicting the free boundaries of cavitation rupture and reformation. Moreover, it is reliable on complex geometries such as linear pad bearings with pockets. For boundary slippage, the multi-linearity algorithm, which follows the critical shear stress criterion, is chosen for its suitability and accuracy for two-dimensional systems.

The first part of the thesis gives mathematical modeling of the Reynolds equation, cavitation, and boundary slippage equations. The Reynolds equation was first modified to include cavitation by complementary variables. The equations relating surface shear stress and surface slip velocities were divided into N number of control equations by the multi-linearity algorithm. Variational inequalities express the relationship between surface shear stress and surface slip velocities.

An alternative novel model for boundary slippage is presented. In this new model, the equations describing the slip velocities and surface shear stresses are divided into three directions instead of the N number of directions. Then these three directions are rotated to find the correct slip angle. Numerical implantation of all mentioned models is explained using the finite element method.

Four different bearing types were used to test the models ; (i) slider bearings, (ii) journal bearings, (iii) slider bearings with pockets to mimic the surface texture, and (iv) squeeze motion. Journal bearings and slider bearings were used to test the no slipcases (i.e., only cavitation effects are simulated) to show that the cavitation model works correctly. The results do match well with the findings in the literature. Different cavitation models and numerical solution methods can explain the minor differences. Then, using the mass conserving LCP cavitation model, both the fixed N-direction slip model and the rotating three-direction slip model were compared with the findings in the literature. Nine different journal bearings and four different slider bearings were used. The hydrodynamic load support and the friction drag on the surfaces were compared. If we look at the results, both the fixed N-direction slip model and the rotating three-direction slip model works in harmony with the LCP cavitation model, giving high accuracy results. In addition, if 16 or more directions are used for the fixed N-direction slip model, there exists no noticeable difference between the rotating three-direction slip model. It reveals that the three-direction slip model successfully predicts the hydrodynamic characteristics of thin films. The models were tested with slider bearings with pockets to study the performance of complex geometric structures. No noticeable difference was observed between the slip models. Lastly, a transient case was studied. The variation of the cavitation radius between two parallel discs in periodic motion, which are brought closer to each other and then removed

apart, has been investigated. No noticeable difference was observed between the different slip models.

These results show that both the N-direction slip and the rotating three-direction slip model presented in this thesis work in harmony with the LCP cavitation model. The two slip models give the same results in all numerical examples with a minimal margin of error, indicating that the novel slip model proposed in this thesis works successfully.

A final test case was made to demonstrate the computational speed difference between the two models. Journal bearing with an eccentricity ratio of 0.6 is chosen. The fixed N-direction slip model was tested with N=3,4,8 and 16. Hydrodynamic load and friction drag values were calculated for each case. Then these values were compared with the results of the rotating 3-direction slip model, and it was found out that for the difference between them to fall below 1 percent, N must be greater than 16. In the case of N=16, the rotating 3-direction slip model is four times faster than the fixed N-direction slip model. These results concluded that the novel rotating 3-direction slip model presented in this paper is faster if the same accuracy is desired.

Several improvements are planned to continue and validate this work in the future. Hydrodynamic characteristics of the bearing when surfaces are coated with superhydrophobic materials have been reported. However, coating surfaces with superhydrophobic materials will bring an increase in cost. Therefore, it is necessary to optimize the surfaces to find the optimum heterogeneous slip/no-slip surface setups. Complex rheology effects such as shear thinning and piezoviscosity [48],[55] are planned to integrate into the numerical model. Future experiments on bearings are planned to verify the numerical model presented in this work.

Bibliography

[1] H. P. Jost, *Lubrication: Tribology; Education and Research; Report on the Present Position and Industry's Needs (submitted to the Department of Education and Science by the Lubrication Engineering and Research) Working Group*. HM Stationery Office, 1966.

[2] K. Holmberg and A. Erdemir, "Influence of tribology on global energy consumption, costs and emissions," *Friction*, vol. 5, no. 3, pp. 263–284, 2017.

[3] B. Bhushan, *Introduction to tribology*. John Wiley & Sons, 2013.

[4] R. Bassani and B. Piccigallo, *Hydrostatic lubrication*, vol. 22. Elsevier, 1992.

[5] Y. Hori, *Hydrodynamic lubrication*. Springer Science & Business Media, 2006.

[6] N. Churaev, V. Sobolev, and A. Somov, "Slippage of liquids over lyophobic solid surfaces," *Journal of Colloid and Interface Science*, vol. 97, no. 2, pp. 574–581, 1984.

[7] O. I. Vinogradova, "Slippage of water over hydrophobic surfaces," *International journal of mineral processing*, vol. 56, no. 1-4, pp. 31–60, 1999.

[8] R. Pit, H. Hervet, and L. Léger, "Friction and slip of a simple liquid at a solid surface," *Tribology letters*, vol. 7, no. 2, pp. 147–152, 1999.

[9] R. Pit, H. Hervet, and L. Leger, "Direct experimental evidence of slip in hexadecane: solid interfaces," *Physical review letters*, vol. 85, no. 5, p. 980, 2000.

[10] Y. Zhu and S. Granick, "Rate-dependent slip of newtonian liquid at smooth surfaces," *Physical review letters*, vol. 87, no. 9, p. 096105, 2001.

[11] Y. Zhu and S. Granick, "Limits of the hydrodynamic no-slip boundary condition," *Physical review letters*, vol. 88, no. 10, p. 106102, 2002.

[12] L. Léger, E. Raphaël, and H. Hervet, "Surface-anchored polymer chains: Their role in adhesion and friction," *Polymers in confined environments*, pp. 185–225, 1999.

[13] S.-Q. Wang, "Molecular transitions and dynamics at polymer/wall interfaces: origins of flow instabilities and wall slip," *Polymers in confined environments*, pp. 227–275, 1999.

[14] M. Tauviqirrahman, W. Ajie, E. YOHANA, M. Muchammad, and J. Jamari, "A study of slip position on improving the hydrodynamic lubrication performance of single-textured bearing using a mass conserving numerical approach," *International Journal of Engineering and Technology*, vol. 8, no. 2, pp. 913–920, 2016.

[15] R. F. Salant and A. E. Fortier, "Numerical analysis of a slider bearing with a heterogeneous slip/no-slip surface," *Tribology Transactions*, vol. 47, no. 3, pp. 328–334, 2004.

[16] A. E. Fortier and R. F. Salant, "Numerical analysis of a journal bearing with a heterogeneous slip/no-slip surface," 2005.

[17] H. Spikes and S. Granick, "Equation for slip of simple liquids at smooth solid surfaces," *Langmuir*, vol. 19, no. 12, pp. 5065–5071, 2003.

[18] H. A. Spikes, "The half-wetted bearing. part 1: extended reynolds equation," *Proceedings of the Institution of Mechanical Engineers, Part J: Journal of Engineering Tribology*, vol. 217, no. 1, pp. 1–14, 2003.

[19] H. A. Spikes, "The half-wetted bearing. part 2: potential application in low load contacts," *Proceedings of the Institution of Mechanical Engineers, Part J: Journal of Engineering Tribology*, vol. 217, no. 1, pp. 15–26, 2003.

[20] A. Strozzi, M. Giacopini, E. Bertocchi, and D. Dini, "Formulation of the tangential velocity slip problem in terms of variational inequalities," *Proceedings of the Institution of Mechanical Engineers, Part J: Journal of Engineering Tribology*, vol. 228, no. 10, pp. 1122–1135, 2014.

[21] G. Bayada, "A fast algorithm for boundary slippage including mass flow conserving cavitation model," *Tribology International*, vol. 118, pp. 71–88, 2018.

[22] L. Biancofiore, M. Giacopini, and D. Dini, "Interplay between wall slip and cavitation: A complementary variable approach," *Tribology International*, vol. 137, pp. 324–339, 2019.

[23] C. Wu and G. Ma, "Abnormal behavior of a hydrodynamic lubrication journal bearing caused by wall slip," *Tribology international*, vol. 38, no. 5, pp. 492–499, 2005.

[24] G. Ma, C. Wu, and P. Zhou, "Multi-linearity algorithm for wall slip in two-dimensional gap flow," *International journal for numerical methods in engineering*, vol. 69, no. 12, pp. 2469–2484, 2007.

[25] G. Ma, C. Wu, and P. Zhou, "Wall slip and hydrodynamics of two-dimensional journal bearing," *Tribology International*, vol. 40, no. 7, pp. 1056–1066, 2007.

[26] G. Ma, C. Wu, and P. Zhou, "Hydrodynamics of slip wedge and optimization of surface slip property," *Science in China Series G: Physics, Mechanics and Astronomy*, vol. 50, no. 3, pp. 321–330, 2007.

[27] J. Cole and C. Hughes, "Oil flow and film extent in complete journal bearings," *Proceedings of the Institution of Mechanical Engineers*, vol. 170, no. 1, pp. 499–510, 1956.

[28] F. Y. Zeidan and J. M. Vance, "Cavitation regimes in squeeze film dampers and their effect on the pressure distribution," *Tribology transactions*, vol. 33, no. 3, pp. 447–453, 1990.

[29] M. Braun and R. Hendricks, "An experimental investigation of the vaporous/gaseous cavity characteristics of an eccentric journal bearing," *ASLE transactions*, vol. 27, no. 1, pp. 1–14, 1984.

[30] D. Sun, D. Brewe, and P. Abel, "Simultaneous pressure measurement and high-speed photography study of cavitation in a dynamically loaded journal bearing," 1993.

[31] S. Diaz and L. San Andre´ s, "A model for squeeze film dampers operating with air entrainment and validation with experiments," *J. Trib.*, vol. 123, no. 1, pp. 125–133, 2001.

[32] C.-P. Ku and J. Tichy, "An experimental and theoretical study of cavitation in a finite submerged squeeze film damper," 1990.

[33] L. Gümbel, "Das problem der lagerreibung," *Mbl. Berlin. Bez. Ver. dtsch. Ing*, vol. 5, pp. 87–104, 1914.

[34] B. Jakobsson, "The finite journal bearing, considering vaporization," *Transactions of Chalmers University of Technology*, vol. 190, 1957.

[35] K.-O. Olsson, "Cavitation in dynamically loaded bearings," *Transactions of Chalmers University of Technology*, vol. 308, 1965.

[36] H. Elrod, "A computer program for cavitation and starvation problems," *Cavitation and related phenomena in lubrication*, vol. 37, 1974.

[37] H. Elrod and M. Adams, "A computer program for cavitation and starvation problems, cavitation and related phenomena in lubrication, dowson, d., godet, m. and taylor, cm eds," 1975.

[38] G. Bayada and M. Chambat, "Analysis of a free boundary problem in partial lubrication," *Quarterly of Applied Mathematics*, vol. 40, no. 4, pp. 369–375, 1983.

[39] G. Bayada and L. Chupin, "Compressible fluid model for hydrodynamic lubrication cavitation," *Journal of Tribology*, vol. 135, no. 4, p. 041702, 2013.

[40] B. Guy, "From a compressible fluid model to new mass conserving cavitation algorithms," *Tribology International*, vol. 71, pp. 38–49, 2014.

[41] M. Giacopini, M. T. Fowell, D. Dini, and A. Strozzi, "A mass-conserving complementarity formulation to study lubricant films in the presence of cavitation," 2010.

[42] L. Bertocchi, D. Dini, M. Giacopini, M. T. Fowell, and A. Baldini, "Fluid film lubrication in the presence of cavitation: a mass-conserving two-dimensional formulation for compressible, piezoviscous and non-newtonian fluids," *Tribology International*, vol. 67, pp. 61–71, 2013.

[43] T. Woloszynski, P. Podsiadlo, and G. W. Stachowiak, "Efficient solution to the cavitation problem in hydrodynamic lubrication," *Tribology Letters*, vol. 58, no. 1, pp. 1–11, 2015.

[44] F. Sahlin, A. Almqvist, R. Larsson, and S. Glavatskih, "A cavitation algorithm for arbitrary lubricant compressibility," *Tribology International*, vol. 40, no. 8, pp. 1294–1300, 2007.

[45] M. S. Plesset, "The dynamics of cavitation bubbles," 1949.

[46] L. Rayleigh, "Viii. on the pressure developed in a liquid during the collapse of a spherical cavity," *The London, Edinburgh, and Dublin Philosophical Magazine and Journal of Science*, vol. 34, no. 200, pp. 94–98, 1917.

[47] J.-P. Franc, "The rayleigh-plesset equation: a simple and powerful tool to understand various aspects of cavitation," in *Fluid dynamics of cavitation and cavitating turbopumps*, pp. 1–41, Springer, 2007.

[48] S. Gamaniel, D. Dini, and L. Biancofiore, "The effect of fluid viscoelasticity in lubricated contacts in the presence of cavitation," *Tribology International*, vol. 160, p. 107011, 2021.

[49] A. Hajishafiee, A. Kadiric, S. Ioannides, and D. Dini, "A coupled finite-volume cfd solver for two-dimensional elasto-hydrodynamic lubrication problems with particular application to rolling element bearings," *Tribology International*, vol. 109, pp. 258–273, 2017.

[50] O. Reynolds, "Iv. on the theory of lubrication and its application to mr. beauchamp tower?s experiments, including an experimental determination of the viscosity of olive oil," *Philosophical transactions of the Royal Society of London*, no. 177, pp. 157–234, 1886.

[51] A. Z. Szeri, *Fluid film lubrication*. Cambridge university press, 2010.

[52] D. Dowson and G. R. Higginson, *Elasto-hydrodynamic lubrication: international series on materials science and technology*. Elsevier, 2014.

[53] A. A. Cannarozzi, "On the resolution of some unilaterally constrained problems in structural engineering," *Computer Methods in Applied Mechanics and Engineering*, vol. 24, no. 3, pp. 339–357, 1980.

[54] R. Ausas, P. Ragot, J. Leiva, M. Jai, G. Bayada, and G. C. Buscaglia, "The impact of the cavitation model in the analysis of microtextured lubricated journal bearings," 2007.

[55] H. Ahmed and L. Biancofiore, "A new approach for modeling viscoelastic thin film lubrication," *Journal of Non-Newtonian Fluid Mechanics*, vol. 292, p. 104524, 2021.